

University of Central Florida

STARS

Electronic Theses and Dissertations

2007

Vacancy Engineered Doped And Undoped Nanocrystalline Rare Earth Oxide Particles For High Temperature Oxidation Resistant Coating

Ranjith Thanneeru
University of Central Florida



Part of the [Materials Science and Engineering Commons](#)

Find similar works at: <https://stars.library.ucf.edu/etd>

University of Central Florida Libraries <http://library.ucf.edu>

This Masters Thesis (Open Access) is brought to you for free and open access by STARS. It has been accepted for inclusion in Electronic Theses and Dissertations by an authorized administrator of STARS. For more information, please contact STARS@ucf.edu.

STARS Citation

Thanneeru, Ranjith, "Vacancy Engineered Doped And Undoped Nanocrystalline Rare Earth Oxide Particles For High Temperature Oxidation Resistant Coating" (2007). *Electronic Theses and Dissertations*. 3380. <https://stars.library.ucf.edu/etd/3380>

**VACANCY ENGINEERED DOPED AND UNDOPED NANOCRYSTALLINE
RARE EARTH OXIDE PARTICLES FOR HIGH TEMPERATURE OXIDATION
RESISTANT COATINGS**

by

RANJITH KUMAR THANNEERU
B. Tech. Indian Institute of Technology, Madras, 2004

A thesis submitted in partial fulfillment of the requirements
for the degree of Master of Science
in the Department of Mechanical, Materials and Aerospace Engineering
in the College of Engineering and Computer Science
at the University of Central Florida
Orlando, Florida

Spring Term
2007

©2007 Ranjith Kumar Thanneeru

ABSTRACT

Rare earth oxides with trivalent lattice dopants have been of great interest to researchers in the recent years due to its potential applications in catalysis and high temperature protective coatings. The ability to store oxygen in rare earths is the basis for catalysis because of the ability to change valence states which causes the presence of intrinsic oxygen vacancies in the crystal lattice. Although, several doped-rare earth oxide systems in micron scale have been investigated, the doping effect in cerium oxide nanoparticles with well characterized particle size has not been studied. The doping of ceria at that small size can be very beneficial to further improve its catalytic properties and alter the high temperature phases in alloy systems. Cost effective room temperature chemical methods are used in the current work to synthesize uniformly distributed undoped and doped (dopants: La, Nd, Sm, Gd, Y and Yb) rare earth oxide nanoparticles.

In the present study, the variation of the properties in nanocrystalline ceria (NC) synthesized by microemulsion method is studied as a function of dopant size and its concentration. To further understand, the role of dopant (cation) size on the oxygen vacancy concentration, doped nanocrystalline oxide powders were analyzed by Raman Spectroscopy, X-ray Diffraction (XRD) and X-ray Photoelectron Spectroscopy (XPS). XRD studies showed that lattice parameter change in nanocrystalline oxide by doping trivalent rare earth elements is largely depending on size of trivalent ions. It showed that by doping larger cations (Gd^{3+} and Y^{3+}) compare to Ce^{3+} causes lattice expansion where as smaller cations (Yb^{3+}) leads to lattice contraction. It also showed that the lattice expansion or contraction is directly proportional to dopant concentration. The results

of Raman Spectroscopy showed that the correlation length decreases resulting in increase in oxygen vacancies for larger trivalent dopants (Sm^{3+} , Gd^{3+} and Y^{3+}). However, the correlation length increases resulting in decrease in oxygen vacancies for smaller trivalent dopants (Yb^{3+}) compare to nanocrystalline ceria.

These nanostructured oxides are further applied to develop high temperature oxidation resistance coatings for austenitic steels. The present study investigates the role of oxygen vacancies in the performance of high temperature oxidation resistance as a function of various trivalent dopants and dopant concentration. NC and La^{3+} doped nanocrystalline ceria (LDN) particles were coated on AISI 304 stainless steels (SS) and exposed to 1243K in dry air for longer duration and subjected to cycling. The results are further compared with that of micro-ceria (MC) coatings. The coated samples showed 90% improvement in oxidation resistance compared to uncoated and MC coated steels as seen from the SEM cross-sectional studies. XRD analysis showed the presence of chromia in both NC and 20 LDN samples which is absent in uncoated steels. From SIMS depth profiles, Fe, Ni depletion zones are observed in presence of LDN coated sample indicating diffusion through the oxide layer. The role of oxygen vacancies in the nanoceria coatings on the early formation of protective chromia layer is discussed and compared to its micron counterpart.

This study helps in understanding the role of oxygen vacancies to protect austenitic stainless steel at high temperature and confirms the oxygen inward diffusion rather cation outward diffusion in rare earth oxide coatings. It also gives an idea to identify the type of dopant and its concentration in nanocrystalline cerium oxide which supplies the critical oxygen partial pressure required at high temperature to form primarily impervious chromia layer.

ACKNOWLEDGMENTS

I wish to thank my faculty advisor, Prof. Sudipta Seal, for providing me the support and giving me an opportunity to work on project related to industrial application during my course of study and research at UCF. Without his motivation and guidance this research work would not have been possible.

I am very grateful to Dr. Jiyu Fang and Dr. Helge Heinrich for being on my thesis committee. I would like to thank Dr. Alfons Schulte and his student Yu Guo for his assistance with the Raman spectroscopic study of the nanoparticles. I also like to thank Dr. J. Schneider and his student H. Koeplin from RWTH (Aachen, Germany) to help with XRD analysis.

I thank Materials Characterization Facility (MCF) at UCF for offering the characterization facilities required for conducting this research work. Also, I would like to acknowledge all the students in the Surface Engineering and Nanotechnology Facility (SNF) and Plasma Lab and my friends for their cooperation and support. Special thanks to Dr. Swanand Patil and Dr. Suresh Babu for useful discussion and their valuable suggestions

I am grateful for financial support by National Science Foundation (CMS: 0548815). Above all, I would like to thank my parents and brother whose unfailing love, support and encouragement made me to achieve this.

TABLE OF CONTENTS

LIST OF FIGURES	ix
LIST OF TABLES	xii
LIST OF ACRONYMS	xiii
CHAPTER 1. INTRODUCTION	1
1.1 Nanomaterials: Importance.....	1
1.2 Cerium Oxide: Applications.....	4
CHAPTER 2. SYNTHESIS OF DOPED AND UNDOPED NANOCRYSTALLINE CERIUM OXIDE	6
2.1 Introduction.....	6
2.2 Literature Review	8
2.3 Microemulsion Process for Nanoparticle Synthesis.....	9
2.3.1 Nanoparticles Synthesis.....	9
2.4 Doped and Undoped Nanocrystalline Cerium Oxide by Microemulsion Process.....	15
2.4.1 Cerium Oxide Nanoparticles Synthesis	17
2.4.2 Doping of Cerium Oxide Nanoparticles with Trivalent Elements.....	18
2.5 Conclusion	23
CHAPTER 3. CHARACTERIZATION OF DOPED AND UNDOPED NANOCERIA PARTICLES	24
3.1 Introduction.....	24
3.2 Effect of Doping with Trivalent Elements.....	26

3.2.1 X-ray Diffraction on doped nanocrystalline cerium oxide	26
3.2.2 Raman Spectroscopic Analysis.....	29
3.2.3 X-Ray Photoelectron Spectroscopy Analysis	38
3.3 Conclusion	45
CHAPTER 4. APPLICATION OF DOPED AND UNDOPED NANOCERIA IN HIGH TEMPERATURE OXIDATION PROTECTION	47
4.1 Introduction.....	47
4.2 Literature Review	49
4.3 Experimental Procedure.....	50
4.3.1 Sample Preparation for SEM analysis	53
4.3.1.1 Sample Preparation for Top Surface Analysis.....	53
4.3.1.2 Sample Preparation for Cross Sectional Analysis	53
4.4 Results and Discussion	54
4.4.1 Oxidation Kinetics	54
4.4.2 Morphological Studies	57
4.4.2.1 Top Surface Morphology	57
4.4.2.2 Cross Section Morphology	61
4.4.3 Phase Identification.....	64
4.4.4 Diffusional Studies.....	65
4.5 Role of Oxygen Vacancies in High Temperature Protection	71
4.6 Conclusion	76
CHAPTER 5. CONCLUSIONS AND FUTURE WORK.....	77
5.1 Conclusion	77

5.2 Future Work	78
REFERENCES	79

LIST OF FIGURES

Figure 2.1 Mechanism of synthesis of nanoparticles using mixing of microemulsions.....	12
Figure 2.2 Mechanism of synthesis of nanoparticles using single Microemulsion	13
Figure 2.3 Ternary phase diagram of water/AOT/isooctane system determined using experimental method.....	16
Figure 2.4 HRTEM images of doped and undoped nanoceria samples. (a) NC, (b) 20 SDN, (c) 20 GDN, (d) 20 YDN and (e) 20 YbDN.....	22
Figure 3.1 (a) XRD spectra of MC, NC, GDN, YDN and YbDN samples (b) Lattice parameter variation of the nanoceria samples as a function of doping amount.....	29
Figure 3.2 (a) Raman spectra of undoped and doped (Sm, Gd, Y and Yb) nanoceria samples (b) Raman peak shift of the nanoceria samples as a function of doping amount.....	36
Figure 3.3 (a) The correlation length and (b) Oxygen vacancies Concentration of the nanoceria samples as a function of doping amount.....	37
Figure 3.4 Peak fitted XPS spectrum of Ce (3d) for (a) Nanoceria (b) 20 GDN (c) 40 GDN (d) 20 YDN (e) 40 YDN (f) 20 YbDN (g) 40 YbDN.....	42
Figure 3.5 Concentration ratio of Ce^{3+} to Ce^{4+} as a function of dopant concentration for dopants Gd, Y and Yb as calculated using equation 10.....	44
Figure 4.1 Dip Coating Process used for coating doped and undoped ceria on AISI 304 SS samples.....	51

Figure 4.2 Weight gain per unit area versus time plots for isothermal oxidation of AISI 304 SS at 1243 K in dry air for 24h.	54
Figure 4.3 SEM micrographs of top oxide scale formed on the (a) NC, (b) 2 LDN, (c) 20 LDN and (d) 40 LDN SS at 1243K (at 5000X).	57
Figure 4.4 The average percentage porosity on the top oxide layer formed on AISI 304 stainless steel coated with NC and 2, 20 and 40 LDN and oxidized at 1243 K for 24 h in dry air.	59
Figure 4.5 EDX spectra of the top oxide scale formed on NC (top) and 20 LDN (bottom) coated SS at 1243 K.	60
Figure 4.6 SEM micrograph of the cross section, line scanning and X-ray mapping of each element of SS samples coated with NC.	61
Figure 4.7 SEM micrograph of the cross section, line scanning and X-ray mapping of each element of SS samples coated with 20 LDN.	62
Figure 4.8 XRD spectra for SS surface (I) uncoated, (II) NC and (III) 20LDN coated samples. Peak identification: (a) Fe-Cr, (b) Cr ₂ O ₃ , (c) Fe ₃ O ₄ and (d) FeCr ₂ O ₄	64
Figure 4.9 SIMS depth profiles of Fe, Ni, Cr and O from the outer surface to the inner surface of oxide scale formed on the NC coated SS.	68
Figure 4.10 SIMS depth profiles of Fe, Ni and Cr from the outer surface to the inner surface of oxide scale formed on the 20 LDN coated SS. The inset shows Fe and Ni depletion zones present in the oxide layer.	70
Figure 4.11 Lattice expansion slope vs. RE ³⁺ ionic radius for Ce _{1-x} RE _x O _{2-y} samples (J. R. McBride et al)	72

Figure 4.12 Fluorite Structure of (a) Ceria (space-group: Fm3m) and (b) $Ce_{1-x}La_xO_{2-y}$ showing the increase in the lattice parameter and the presence of oxygen vacancies by doping La into nanocrystalline ceria. 73

LIST OF TABLES

Table 2.1 Synthesis Parameters of Doped and Undoped Nanoceria	20
Table 3.1 Calculated correlation length (L) values for doped (Sm, Gd, Y and Yb) and undoped nanoceria	34
Table 3.2 Calculated Defect Concentration in doped (Sm, Gd, Y and Yb) and undoped nanoceria	34
Table 3.3 XPS binding energies of individual peaks of the Ce(3d) spectrum for undoped and doped nanoceria	43
Table 4.1 Parabolic rate constants or K_p values for oxidation of bare and pure and doped ceria-coated AISI 304 stainless steel samples at 1243 k for 24h	56
Table 4.2 Calculated oxygen vacancy concentration in ceria doped with lanthanum	74

LIST OF ACRONYMS

AOT	Sodium bis(2-ethylhexyl) sulphosuccinate
GDN	Gadolinium Doped Nanoceria
LDN	Lanthanum Doped Nanoceria
MC	Micro Ceria
NC	Nanocrystalline Ceria
NDN	Neodymium Doped Nanoceria
SDN	Samarium Doped Nanoceria
SEM	Scanning Electron Microscopy
SIMS	Secondary Ion Mass Spectroscopy
SS	Stainless Steel
STM	Scanning Tunneling Microscopy

TEM	Transmission Electron Microscopy
UV	Ultraviolet
W/O	Water in Oil
W_o	Water to Surfactant molar ratio ($[H_2O]/ [AOT]$)
XPS	X-ray Photoelectron Spectroscopy
XRD	X-Ray Diffraction
YbDN	Ytterbium Doped Nanoceria
YDN	Yttrium Doped Nanoceria

CHAPTER 1. INTRODUCTION

1.1 Nanomaterials: Importance

The first mention of some of the distinguishing concepts in nanotechnology was in “There’s Plenty of Room at the Bottom” a talk given by Nobel laureate Richard Feynman at an American Physical Society meeting at California Institute of Technology on December 29, 1959. Feynman described about this technology as manipulating and controlling at the atoms and molecular level, using one set of precise tools to build and operate another proportionally smaller set, so on down to the needed scale. In the course of this, he also noted, scaling issues would arise from the changing magnitude of various physical phenomena: gravity would become less important, Van der Waals attraction and surface tension would become more important, etc. This basic idea appears feasible, and exponential assembly enhances it with parallelism to produce a useful quantity of end products. Since then, there have been revolutionary developments in physics, chemistry and biology over the years.

The term "nanotechnology" was defined by Professor Norio Taniguchi in a 1974 paper as follows: "'Nano-technology' mainly consists of the processing of, separation, consolidation, and deformation of materials by one atom or one molecule." In the 1980s the basic idea of this definition was explored in much more depth by Dr. K Eric Drexler, who promoted the technological significance of nano-scale phenomena and devices through the books “Engines of Creation: The Coming Era of Nanotechnology” and “Nanosystem: Molecular Machinery, Manufacturing, and Computation”, and so the term acquired its current sense.

The two major developments; the birth of cluster science and the invention of scanning tunneling microscope (STM) in the early 1980s are the starting points of Nanotechnology and nanoscience. This development led to the discovery of fullerenes in 1986 and few years later the discovery of carbon nanotubes. In another development, the synthesis and properties of semiconductor nanocrystals was studied. This led to a fast increasing number of metal oxide nanoparticles of quantum dots.

A unique aspect of nanotechnology is the vastly increased ratio of surface area to volume present in many nanoscale materials which opens new possibilities in surface-based science, such as catalysis. When the dimensions of a material are decreased from macroscale to nanoscale, its properties such as electronic conductivity, optical absorption, chemical reactivity, mechanical properties etc. change significantly. A number of physical phenomena become noticeably pronounced as the size of the system decreases. These include quantum mechanical effects and statistical mechanical effects, for example the “quantum size effect” where the electronic properties of solids are altered with great reductions in particle size. This effect does not come into play by going from macro to micro dimensions. However, it becomes dominant when the nanometer size range is reached. Additionally, a number of physical properties change when compared to macroscopic systems. One example is the increase in surface area to volume of materials which imparts a serious change of surface energy and surface morphology. All these factors alter the basic properties and the chemical reactivity of the nanomaterials. The changes in the properties cause tunable wavelength, improved catalytic ability and better burning rate for propellants and so on. This catalytic activity also opens potential risks in their interaction with biomaterials.

Although nanotechnology is now well-known, it is just emerging from fundamental research to the industrial application and still remains in its pre-exploration stage. Further research in nanotechnology promises breakthroughs in materials and manufacturing, biotechnology, medicine and healthcare, nanoelectronics, and information technology. The discovery of novel materials, processes, and phenomena at the nanoscale, as well as the development of new experimental and theoretical techniques for research provide fresh opportunities for the development of innovative nanosystems and nanostructured materials. Nanostructured materials can be made with unique nanostructures and properties. This field is expected to open new venues in science and technology.

Widespread use and search for technological applications of nanocrystalline materials requires the availability of large quantities of well characterized material with reproducible properties; and this needs to be done economically. Even though nanocrystalline powders are now more expensive than the more commercially available coarse-grained powders, greater usage and tonnage production will bring down the cost. In this respect, one can recall the case of metallic glass tapes produced by the rapid solidification processing, now being used commercially for transformer core laminations. While the tapes costed US\$ 300 per kg in late 1978 when they were first produced they now cost only about \$2. A solution to the barriers for commercial utilization of nanocrystalline materials can be identification of well-defined applications for these materials and this can be a driver for accelerated research. In this context, development of novel synthesis methods to produce these materials in commercially viable quantities is an urgent necessity. Simultaneously, the properties of the existing materials need to be significantly improved. Applications of nanostructured materials are in their infancy, but the explosion of interest in this field is expected to provide an early maturation.

1.2 Cerium Oxide: Applications

Although cerium is a rare earth element, it is relatively abundant in the earth's crust. Among the lanthanides, it is the most abundant, and among the 78 common elements in the earth's crust, it ranks 25th in occurrence at an average distribution of 20 to 60 ppm. After europium, cerium is the most reactive of the rare earth metals, easily oxidizing at room temperature. While most of the rare earths exist in trivalent state, cerium also occurs in +4 state and may flip-flop between the two in a redox reaction. It is established that cerium oxides make excellent oxygen buffers, because of its redox capacity. As a result of alterations in cerium oxidation state, cerium oxide forms oxygen vacancies, or defects, in the lattice structure, by loss of oxygen and/or its electrons. The valence and defect structure of cerium oxide is dynamic and may change spontaneously or in response to physical parameters such as temperature, presence of other ions, and oxygen partial pressure (pO_2).

Although cerium oxide at nanoscale has chemical properties similar to its bulk state to some extent, there are many different characteristics can be observed at the nanoscale. For example, Raman spectra of cerium oxide nanoparticles are very different from micro-sized cerium oxide particles. Additionally, at the nanoscale, the surface area of cerium oxide particles is dramatically increased which not only increases oxygen exchange but also makes it easy for redox reactions.

In view of the importance of nanoceria in various industrial applications, the primary objective of this work is to synthesize controlled sized cerium oxide nanoparticles and doped nanoceria particles; understand the alteration of basic properties of cerium oxide nanoparticles by doping different trivalent rare earth elements and study its effect in high temperature oxidation

resistance of Stainless Steel. This study is based on the redox property of cerium oxide which forms oxygen vacancies, or defects, in the lattice structure, by loss of oxygen and/or its electrons. We also studied how the lattice parameter, oxygen vacancy concentration and the oxidation states of cerium changes by doping with different trivalent rare earth elements.

CHAPTER 2. SYNTHESIS OF DOPED AND UNDOPED NANOCRYSTALLINE CERIUM OXIDE

2.1 Introduction

The biggest challenge for today's science and technology is production of nanoscale materials. Although the progress in this field has been very impressive in recent years, there needs to be lot to understand the properties of these systems and to achieve good control of the nanostructure of these materials.

Nanocrystalline structures are not really very new and were detected in samples of lunar soils. Many conventional catalytic materials are based on very fine microstructures. Nanostructures formed chemically under ambient conditions can also be found in natural biological systems from seashells to bone and teeth in the human body. These materials are notable in that they are simultaneously hard, strong, and tough. Therefore, a number of investigations have been conducted to mimic nature (biomimetics) and also artificially synthesize nanostructured materials and study their properties and behavior. These investigations have clearly shown that one could engineer the properties of nanocrystalline materials through control of microstructural features, more specifically the grain size.

Synthesis and assembly strategies of nanoparticles and nanomaterials accommodate precursors from liquid, solid, or gas phase. They employ both chemical and physical deposition approaches; and similarly rely on either chemical reactivity or physical compaction to integrate nanostructure building blocks within the final material structure.

The "bottom-up" approach of nanomaterials synthesis first forms the nanostructured building blocks (nanoparticles) and then assembles them into the final material. An example of this approach is the formation of powder components through aerosol techniques and then the compaction of the components into the final material. These techniques have been used extensively in the formation of structural composite nanomaterials.

One "top-down" approach begins with a suitable starting material and then "sculpts" the functionality from the material. This technique is similar to the approach used by the semiconductor industry in forming devices out of an electronic substrate (silicon), utilizing pattern formation (such as electron beam lithography) and pattern transfer processes (such as reactive ion etching) that have the requisite spatial resolution to achieve creation of structures at the nanoscale. This particular area of nanostructure formation has tremendous scope and is a driving issue for the electronics industry. Another top-down approach is "ball-milling," the formation of nanostructure building blocks through controlled, mechanical attrition of the bulk starting material. Those nano building blocks are then subsequently assembled into a new bulk material.

In fact, many current strategies for material synthesis integrate both synthesis and assembly into a single process, such as characterizes chemical synthesis of nanostructured materials. The degree of control required over the sizes of the nanostructure components, and the nature of their distribution and bonding within the fully formed material varies greatly, depending on the ultimate materials application. Achieving selective optical absorption in a material may allow a wide range of sizes of the component nanostructure building blocks, while quantum dot lasers or single electron transistors require a far tighter distribution of size of the nanostructure

components. Compaction methods may provide excellent adhesion for nanocomposite materials of improved structural performance (e.g., ductility), but such interfaces may be unsatisfactory for electronic materials.

2.2 Literature Review

Several techniques have been developed for the synthesis of various types of nanoparticles. These include inert gas condensation, mechanical alloying, spray conversion processing, severe plastic deformation, electro-deposition, rapid solidification from the melt, physical vapor deposition, chemical vapor processing, co-precipitation, sol-gel processing, sliding wear, spark erosion plasma processing, auto-ignition, laser ablation, hydrothermal pyrolysis, thermophoretic forced flux system, and devitrification of amorphous phases. Actually, in practical any method capable of producing very fine grain-sized materials can be used to synthesize nanocrystalline materials. Each of these methods has advantages and disadvantages and one should choose the appropriate method depending upon the requirements.

The choice of the method depends upon the ability to control the most important feature of the nanocrystalline materials, viz., the microstructural features (grain size, layer spacing, etc.). Precipitation reactions in microemulsions offer a novel and versatile technique for the synthesis of a wide variety of nanophase materials with the ability to control precisely the size and shape of the particles formed.

2.3 Microemulsion Process for Nanoparticle Synthesis

The term microemulsion was first used by Jack H. Shulman, a professor of chemistry at Columbia University, in 1959. Alternative names of these systems are often used, such as transparent emulsion, swollen micelle, micellar solution and solubilized oil. Microemulsion is a special class of colloidal solutions with very small droplets of the dispersing phase stabilized by the surfactant molecules, spontaneously arranged as a monolayer between the two immiscible phases (water and oil), to give optically transparent solution. It is defined as an isotropic and thermodynamically stable single-phase system that consists of three components: water, oil, and an amphiphilic molecule, called surfactant. The surfactant molecules form a monolayer at the interface between oil and water, with the hydrophobic tails of the surfactant molecules dissolved in the oil phase and hydrophilic head groups in the aqueous phase. The small droplets formed by the spontaneous arrangement of surfactant molecules at the water-oil interface are called micelles. These droplets may either consist of water or oil. Two main categories for microemulsions are direct and reverse phase, respectively referring to oil in water (dispersant medium) and water in oil (dispersant medium) systems.

2.3.1 Nanoparticles Synthesis

Water-in-oil (W/O) microemulsion technique has become very powerful tool to synthesize monodisperse nanoparticles of various kinds, including dye-doped Nanoparticles, magnetic nanoparticles, semiconductor Q-dots etc. at room temperature in recent years. The beauty of the W/O microemulsion technique is its versatility. The water nanodroplets surrounded by surfactant molecules present in the bulk oil phase serve as nanoreactors for the synthesis of nanoparticles. Nanoparticles precursors (e.g. chemical reagents) undergo chemical reaction inside the

nanoreactor to form nanoparticles, following atom-by-atom integration mechanism. This results in the formation of spherical nanoparticles as the shape of the water pool is spherical. The size of the water pool in the oil phase greatly influences the size of the nanoparticles. Thus, the size of the spherical nanoparticles can be controlled and tuned by changing the size of the water pool (W_0 value, the water-to-surfactant molar ratio). In general, increasing the W_0 value increases the particle size.

A variety of “tailor-made” nanoparticles such as core-shell, doped nanoparticles etc. can be synthesized by microemulsion method. It is also possible to synthesize monodisperse nanoparticles as small as a couple of nanometers to a several hundreds of nanometers by controlling the synthesis parameters.

There are two ways to synthesize nanoparticles using the W/O microemulsion method. They are (i) mixing of two microemulsions (microemulsion A and microemulsion B) and (ii) using single microemulsion (microemulsion A). Mixing of microemulsions contain the reactants necessary for the preparation of desired particles. The reaction is shown schematically in Figure 2.1. It needs lot of care while using identical microemulsion systems for each reactant (precursor and precipitating agent) in order to avoid the complexities. The reaction takes place when the micelles containing the reacting species come into contact with each other either by collision or by coalescence. The precipitate particle is confined to the interior of the microemulsion droplets. This is the main principle utilized in the nanoparticle synthesis. When the chemical reaction rate is fast, the overall rate of the formation of the particles is controlled by the rate of coalescence of the microemulsion droplets containing the reactants. A relatively rigid interface decreases the rate of coalescence leading to slower rate of reaction while a less rigid interface in the

microemulsion enhances it. The structure of oil, surfactant, co-surfactant and the ionic strength of the aqueous phase affect the interface rigidity and one can control the kinetics of the reaction by controlling the rigidity of the interface. Figure 2.1 shows the formation of nanoparticles by using two microemulsions, microemulsion A containing the precursor and the microemulsion B containing the precipitating or reducing agent. The exchange of the reactants takes place after collision of the droplets, in reality the situation is quite complex because of the influence of various factors like viscosity, interface rigidity, mobility of the droplets etc. There are several kinetic models proposed in order to explain the particle formation process in microemulsion systems.

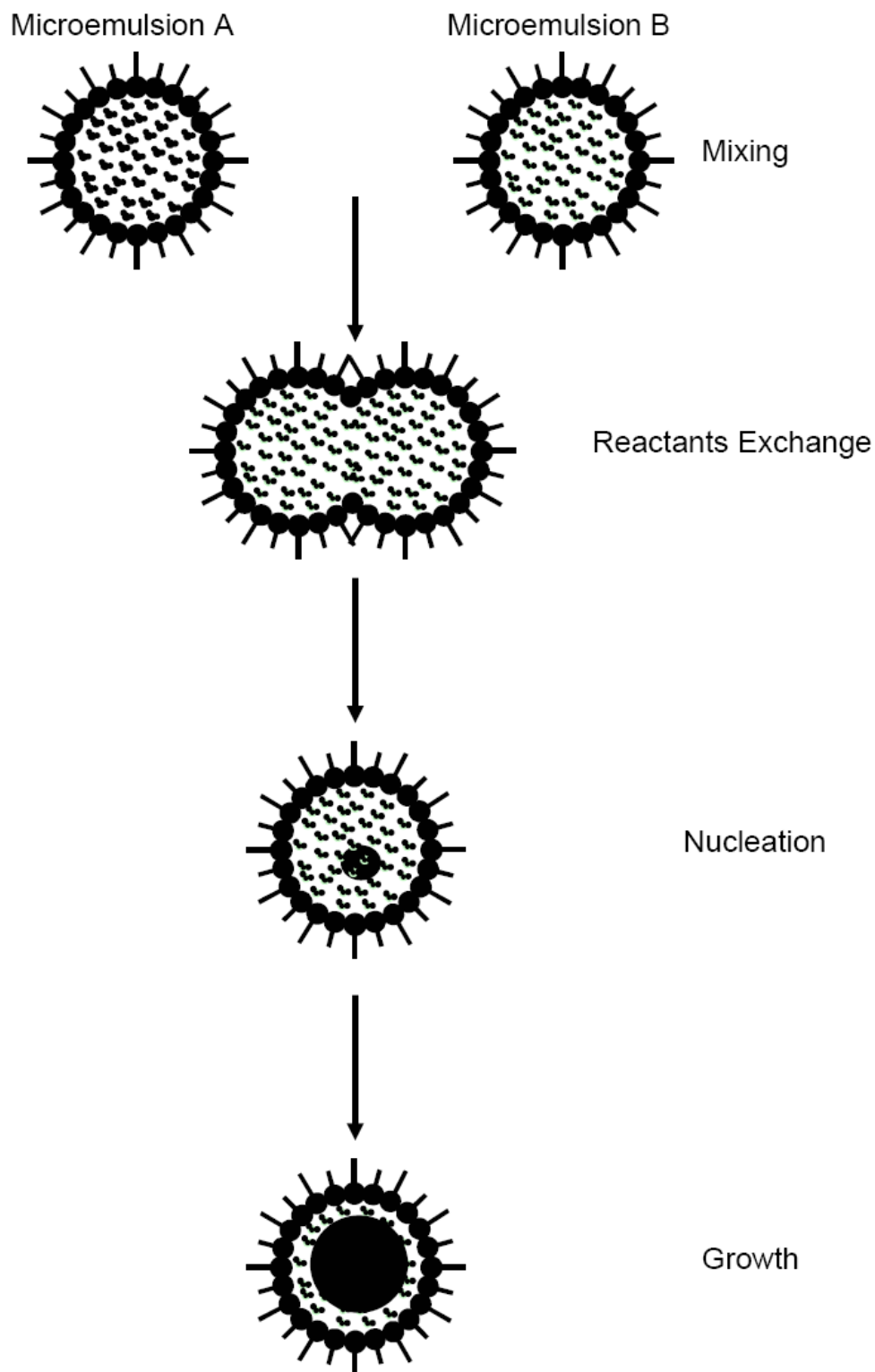


Figure 2.1 Mechanism of synthesis of nanoparticles using mixing of microemulsions

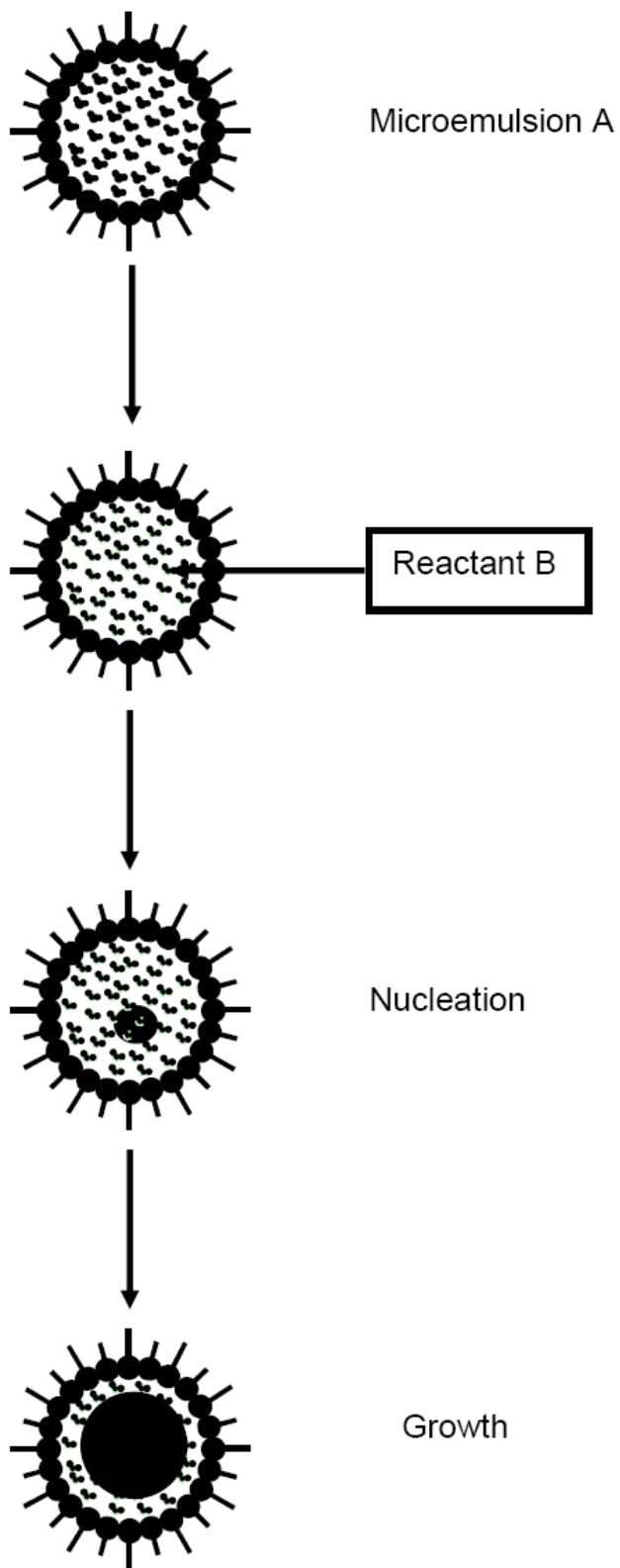


Figure 2.2 Mechanism of synthesis of nanoparticles using single Microemulsion

The nanoparticles can also be synthesized in a microemulsion by adding a precipitating or reducing agent in the form of a liquid or a gas to the microemulsion containing the primary reactant dissolved in its aqueous core. The chances of particle growth in this system due to collision of microemulsion droplets are minimized because of the increased interface stability. Initially, the precipitation or reducing agent will be accessible to the water core of the microemulsion due to the percolation. Subsequently, nuclei of the precipitate are formed inside the water core, which eventually grow till the precipitation or reduction reaction is almost completed inside the microemulsion droplet. Therefore, the size of the final particles will be limited by the size of the water droplet which acts as the nanoreactor in such cases. Mostly, the diameter of the particle formed inside the water droplet is almost equal to the size of the water droplet itself. The reaction is shown schematically in Figure 2.2. Such percolation of the precipitating or reducing agent has been reported for synthesis of various metal-boride and metal-oxide nanoparticles.

Nanoparticles synthesis using the microemulsion technique is a cost effective room temperature chemical synthesis and offers advantages over other techniques. It does not require extreme temperature or pressure conditions; it can be used, in principle, with almost all chemical reactions that have been developed to obtain particles in homogeneous solutions; and it does not require special equipment. But still it is limited as a laboratory technique and different schemes have been proposed to extend this technique to industrial scales.

2.4 Doped and Undoped Nanocrystalline Cerium Oxide by Microemulsion Process

Nanocrystalline ceria particles have been prepared by hydrothermal^{1, 2}, sol-gel³ and microemulsion^{4, 5} methods. The sol-gel and microemulsion methods are useful in coating large size and complex geometry by dipping, spraying, spinning or electrophoresis. However, a major problem associated with preparation of nanoparticles is agglomeration. The particle size is dependent on the concentration of the water solubilized with micelle⁶ while the particle morphology and size distribution is dependent on solubilized state of water⁶.

Moreover, there is a strong tendency of the particles to agglomerate which is resulted from the high surface area of nanocrystalline particles. Bonding by London-Van der Waals forces of attraction causes nanocrystalline particles to form agglomerates⁷. Due to agglomeration, the beneficial effect of the nanosize particles is usually lost. Therefore, it is critical to synthesize non-agglomerated nanocrystalline cerium oxide particles in order to develop coating materials for improvement of high temperature oxidation resistance of the alloys. The present study utilizes the water in oil (W/O) microemulsion method to produce spherical cerium oxide nanoparticles with a controlled particle size.

Reverse micelles form by coordinating surfactant molecules, when water is added to a solution of a non-polar solvent (hydrocarbon) and surfactant (surfactant heads forming the interior of the micelle). The reverse micelles formed in this way have been advantageously used for the synthesis of nanoparticles. Sodium bis (2-ethylhexyl) sulfosuccinate (AOT) is a popular surfactant in reverse micelle applications because of its ability to solubilize relatively large amounts of water in a variety of hydrophobic organic solvents and to form thermodynamically

stable reverse micelles and microemulsions. A typical phase diagram of water/AOT/isooctane system (Figure 2.3) determined using the experimental method by Tamamushi and Watanabe shows the large W/O region, which is useful for nanoparticles synthesis.

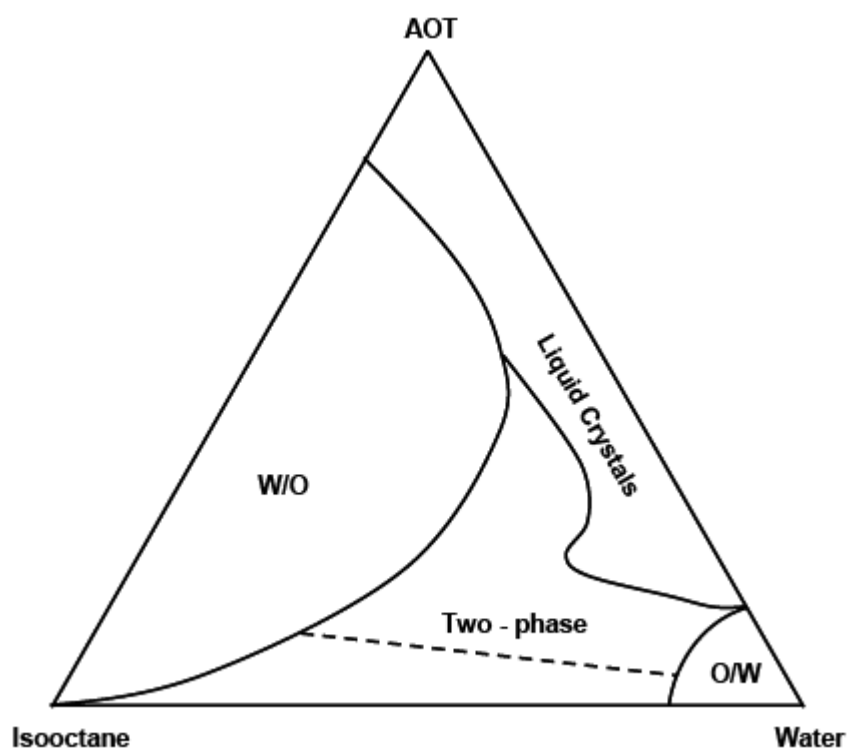


Figure 2.3 Ternary phase diagram of water/AOT/isooctane system determined using experimental method.

AOT is an anionic surfactant with two hydrocarbon chains and does not require co-surfactant to enable to form microemulsion. Therefore, it has been widely used for the synthesis of nanoparticles of various metals as well as oxides. The microemulsion system consisting of toluene or isooctane as oil and AOT as surfactant was utilized in the present study for the synthesis of cerium oxide nanoparticles. In the present study, doping of nanoparticles with no particle size variation was synthesized for further characterization and application. The details of the experiments and the results are discussed in the following sections.

2.4.1 Cerium Oxide Nanoparticles Synthesis

Reverse micelles are used as nanoreactors to synthesize nanoparticles as mentioned earlier. These reverse micelles consist of aqueous droplets of small size that are separated from the bulk organic phase by a monolayer of surfactant. The water pool diameter is believed to govern the size of the reverse micelle, characterized by the molar ratio (W_0), of water to surfactant ($[\text{H}_2\text{O}]/[\text{AOT}]$). The size of micelle is directly proportional to molar ratio (W_0) of water to surfactant. Particle size of the nanoparticles is controlled by the size of the reverse micelle as the nanoparticles are formed in the interiors of the reverse micelle.

AOT was dissolved in toluene (1gm in 100ml) to obtain an AOT/toluene stock solution. A 5ml of 0.1M aqueous cerium nitrate solution was added drop wise to the AOT/toluene solution under magnetic stirring. All the chemicals were obtained from Aldrich Chemicals Company Inc. and used without further purification. 5ml of 0.5N ammonium hydroxide was then added to the reverse micellar solution to obtain the cerium oxide nanoparticles. The solution was kept standstill after completion of reaction to obtain a stable yellow sol containing cerium oxide nanoparticles as a top layer. Excess water phase at the bottom was removed.

The cerium oxide nanoparticles were precipitated from the micellar solution by addition of excess amount of ammonium hydroxide. The precipitated nanoparticles were washed several times with acetone and water and the obtained powder was then dried at 100°C for 2h.

2.4.2 Doping of Cerium Oxide Nanoparticles with Trivalent Elements

Cerium oxide nanoparticles were studied for various catalytic applications due to its ability to easily absorb and release oxygen. The ability to store oxygen is a result of cerium's ability to change valence states and the presence of intrinsic O vacancies in the Ceria lattice. Oxygen vacancies are created in nanoceria for replacement of each two Ce^{4+} sites by two trivalent rare-earth ions in the ceria crystal lattice in order to maintain electrostatic charge neutrality. These vacancies increase O diffusion and thereby increase the ease with which the material can absorb and release O.

Although researchers have studied several doped-Ceria systems, the doping effect in cerium oxide nanoparticles with well characterized particle size has not been studied. The doping of trivalent elements into ceria at that small size can be very beneficial to further improve its catalytic properties. Therefore, the doping effect of mono-disperse cerium oxide nanoparticles with varying amounts of trivalent rare earth elements (Sm, Gd, Y and Yb) for controlled particle size was studied.

All the chemicals were obtained from Aldrich Chemicals Company Inc. and used without further purification. Doped nanocrystalline cerium oxide particles were synthesized by the same microemulsion system (used to synthesize cerium oxide nanoparticles) consisting of AOT, toluene and. Cerium nitrate, with corresponding nitrates (lanthanum nitrate, neodymium nitrate, samarium nitrate, gadolinium nitrate, yttrium nitrate and ytterbium nitrate) were used as the precursors while ammonium hydroxide was used as a co-precipitating agent. The precursors

were mixed with different N_{RE}/N_{Ce} atomic ratios, where RE = La or Nd or Sm or Gd or Y or Yb.

The dopant percentage was determined by the formula:

$$\text{Atomic \% dopant} = (100 \cdot N_{RE}) / (N_{Ce} + N_{RE}) \quad (1)$$

The details of the synthesis parameter for doped and undoped nanoceria are given in Table 2.1.

The synthesis process was the same as that explained in section 2.4.1. In this method LDN, NDN, SDN, GDN, YDN and YbDN solutions were synthesized and SDN, GDN, YDN and YbDN powers were prepared as mentioned in 2.4.1 to characterize the change in properties of the NC with type of dopant.

Table 2.1 Synthesis Parameters of Doped and Undoped Nanoceria

Sample	Amount of dopant (at%) in Ceria	Weight (g) in 5ml Distilled Water	
		Ce(NO ₃) ₃ 6H ₂ O	Nitrates (hydrated) of the corresponding dopant
NC	0	0.2170	---
2LDN	2	0.2130	4.33x10 ⁻³
20LDN	20	0.1736	0.0433
40LDN	40	0.1302	0.0866
20NDN	20	0.1736	0.0438
40NDN	40	0.1302	0.0876
20SDN	20	0.1736	0.0445
40SDN	40	0.1302	0.0889
20GDN	20	0.1736	0.0464
40GDN	40	0.1302	0.0928
20YDN	20	0.1736	0.0384
40YDN	40	0.1302	0.0768
20YbDN	20	0.1736	0.0449
40YbDN	40	0.1302	0.0898

Figure 2.4 shows the bright field HRTEM micrographs of NC and all 20 atomic % doped NC samples exhibiting near-spherical 3-5nm particles with uniform particle size distribution. As W_0 is kept constant in undoped and doped nanoceria samples synthesis, same particle size is expected for all doped ceria samples. The selected area diffraction patterns shown in the inset of the micrographs of undoped and doped nanoceria samples indicate that fluorite structure is maintained even after doping larger and smaller trivalent ions in nanoceria.

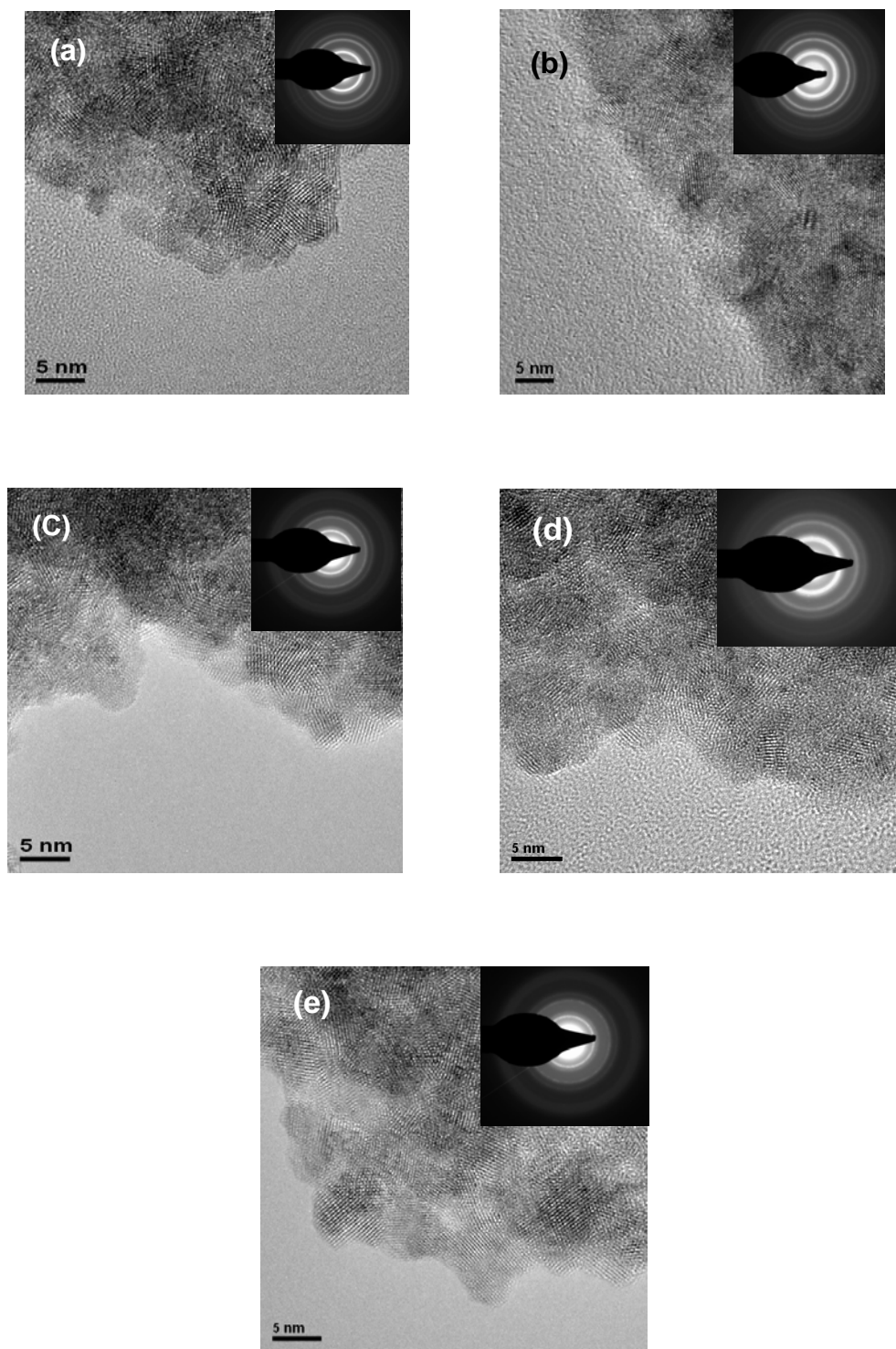


Figure 2.4 HRTEM images of doped and undoped nanoceria samples. (a) NC, (b) 20 SDN, (c) 20 GDN, (d) 20 YDN and (e) 20 YbDN

2.5 Conclusion

- Reverse microemulsion method was used to synthesize undoped and doped (LDN, NDN, SDN, GDN, YDN and YbDN) nanocrystalline cerium oxide particles in order to obtain precise particle size.
- LDN and NDN solutions were synthesized to study and compare the high temperature oxidation protection of stainless steel and results were compared with NC and MC coatings.
- SDN, GDN, YDN and YbDN powders were prepared from the corresponding doped ceria solutions synthesized by microemulsion method to analyze the change in the properties (oxygen vacancies, lattice parameter) of doped NC with respect to dopant size and its concentration.
- HRTEM micrographs of NC and doped ceria (20 SDN, 20 GDN, 20 YDN and 20 YbDN) samples indicate uniform particle size (3-5nm) for all samples and also the diffraction pattern shows retaining of fluorite crystal structure of nanoceria even after doping larger or smaller trivalent ions in nanocrystalline cerium oxide lattice.

CHAPTER 3. CHARACTERIZATION OF DOPED AND UNDOPED NANOCERIA PARTICLES

3.1 Introduction

Materials in nanometer dimensions are very much interest to scientists and technologists from various disciplines and are deeply involved in understanding the novel properties of them. Nanoparticles are different from their bulk counterparts not only in shapes and structures but also in their physical and chemical properties. The radical change in physicochemical properties of nanocrystalline materials with respect to their bulk counterparts, because of their high surface energy, is a subject of intensive investigation. Numerous efforts are ongoing to use such phenomenon advantageously for not only enhancing the performance of the existing materials but also for novel applications.

Nanostructured materials have attracted much attention due to their reported unique structure and physical properties attributed to the grain boundary and grain-size dependent non-stoichiometry. Many researchers have studied structural and physical properties of metal clusters and semiconducting nanoparticles prepared in many ways. A number of studies have shown that materials with grain sizes less than 100 nm exhibit optical, electrical, catalytic and mechanical properties that are different from those observed for conventional microcrystalline specimens. But structural and physical properties of oxide nanoparticles less than 10nm are rarely investigated, because of the difficulties in controlling monodisperse particle size distribution at that range. The ability to enhance the properties by controlling the particle size may lead to

potentially useful technological applications of nanocrystalline oxides in gas sensors, fuel cells, ionic membranes and many more new applications.

Cerium oxide is an important technological ceramic material whose electrical properties are strongly related to the microstructure. It was observed that an enhancement of about four orders of magnitude in electronic conductivity when the microstructure changed from the micro- to nanocrystalline region. This effect was probably attributed to extended interfacial area and reduced enthalpy for defect formation. Recent work has shown that cerium oxide films with ultrafine grain size can greatly improve the resistance of metals and alloys to high temperature oxidation.

The physical properties of nanocrystalline cerium oxide are different (due to increase in defect concentration) than that of bulk or microcrystalline cerium oxide, it is very important to study the variation in these properties in nanoparticle range. This can help to find the required properties of nanocerium for specific applications. In this chapter, the studies related to the fundamental properties of nanocrystalline cerium oxide with different dopant size are presented. The objective was to analyze the properties such as lattice parameter and defects concentration of the cerium oxide nanoparticles as a function of dopant size and its concentration. Raman Spectroscopy and X-ray diffraction (XRD) techniques were carried out to analyze the change in the properties of doped nanocrystalline ceria (with different dopant size) with undoped nanocerium.

3.2 Effect of Doping with Trivalent Elements

Oxygen vacancies are introduced by doping trivalent rare earth elements in nanocrystalline cerium oxide. The objective of this study was to change the oxygen vacancies concentration in cerium oxide nanoparticles by doping different sizes of trivalent elements. As Sm, Gd, Y and Yb cause change in lattice parameter of ceria for a large doping concentration range⁸, they were selected as dopants for ceria nanoparticles synthesized using the microemulsion technique. As discussed in 2.4, we were able to synthesize doped ceria nanoparticles of the controlled particle size for different doping concentrations using the microemulsion process. The synthesized nanoparticles were used for further analysis for changes in lattice parameter and defects concentration, studied using XRD and Raman spectroscopy.

3.2.1 X-ray Diffraction on doped nanocrystalline cerium oxide

X-Ray Diffraction technique (Rigaku model: Cu K_{α1} radiation) was used to find the lattice parameter change induced by doping different trivalent ions in nanocrystalline cerium oxide. The data were recorded at a scan rate of 0.24 degree/min with a step size of 0.01. The peaks can be indexed to the fluorite structure of cerium oxide.

The d-spacing of the different planes was calculated using the Bragg's equation:

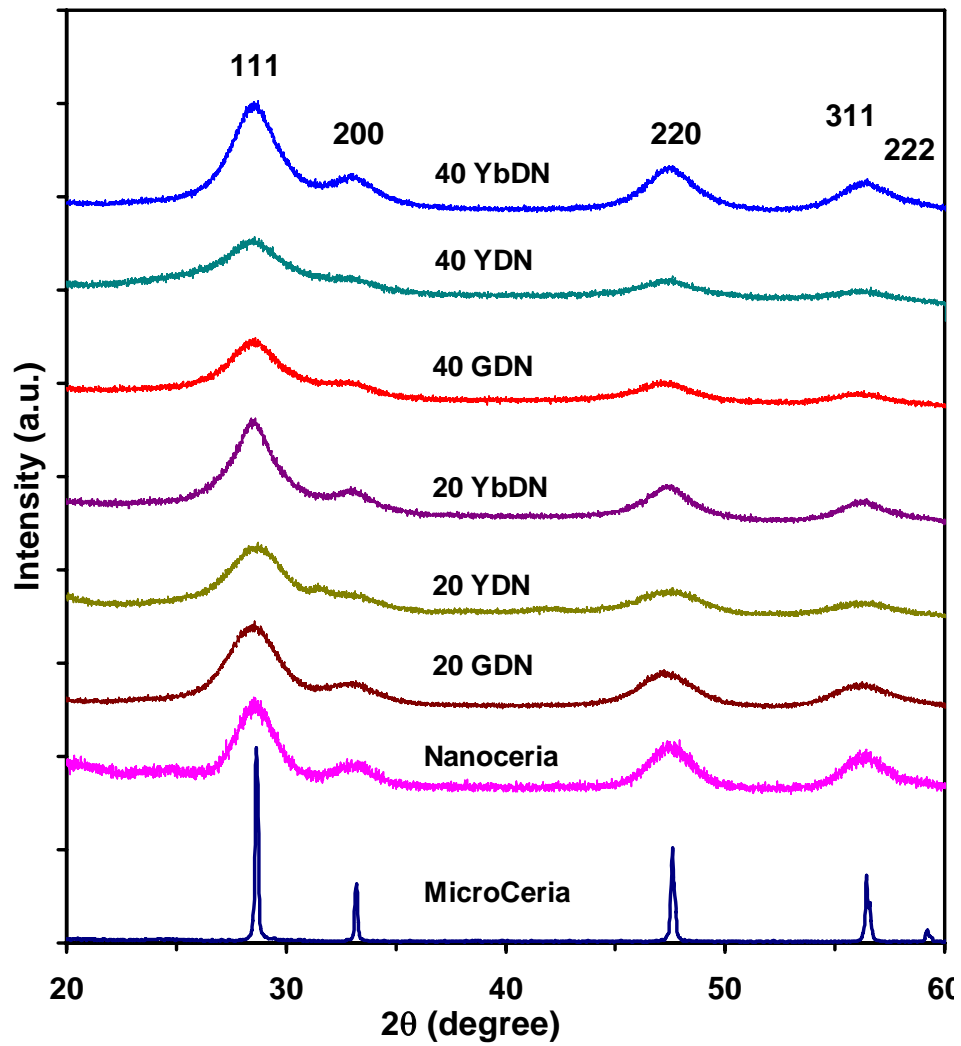
$$n\lambda = 2d\sin\theta \quad (2)$$

where λ is wavelength of X-rays (Cu-K_{α1} = 1.54056 nm), θ is the diffraction angle and $n = 1$. The lattice parameter, a , was further calculated using the relation between d-spacing and lattice parameter ‘a’ as:

$$a = d / (h^2 + k^2 + l^2)^{1/2} \quad (3)$$

Figure 3.1 (a) shows the XRD pattern of GDN, YDN and YbDN samples along with undoped NC and MC samples. The broadened peaks in all the diffractograms confirm the nanocrystalline nature of the synthesized powder samples and the peaks can be indexed to the fluorite structure of cerium oxide. The absence of the additional peaks related to oxides of Gd, Y and Yb in respective doped ceria samples indicate the formation of a single phase $Ce_{1-x}RE_xO_{2-y}$ type solid solution for the full doping range.

The lattice constant for all the samples was measured by fitting the peaks using PeakFit (Version 4.0) software. Figure 3.1 shows the change in the lattice constant with the dopant concentration. The lattice constant shifts shown in Figure 3.1 (b) can be directly correlated with the ionic size of the dopants; the larger or smaller dopants will dilate or contract the lattice, respectively, with the amount of change in lattice constant being approximately proportional to the ionic size of trivalent rare earth element. As the ionic radius of Gd^{3+} is larger than that of Y^{3+} , the lattice constant is larger for all the Gd-doped samples compared to the corresponding Y-doped samples. It also indicates that doping smaller trivalent ions (Yb^{3+}) contract the ceria lattice and the lattice contraction is approximately proportional to trivalent dopant size.



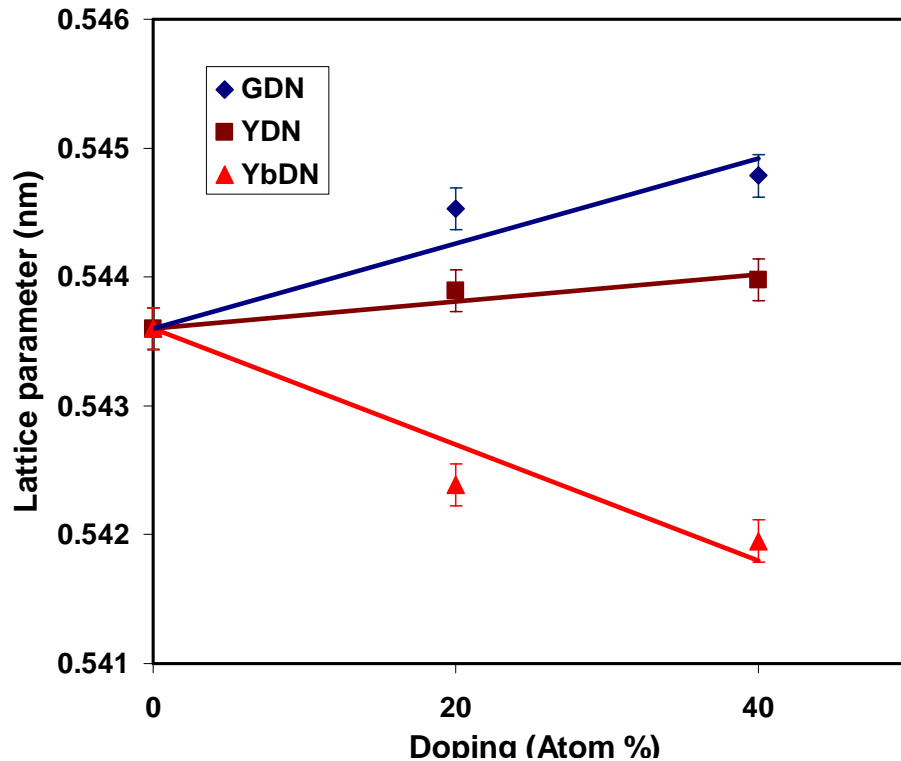


Figure 3.1 (a) XRD spectra of MC, NC, GDN, YDN and YbDN samples (b) Lattice parameter variation of the nanoceria samples as a function of doping amount.

3.2.2 Raman Spectroscopic Analysis

Raman scattering is a non-destructive and rapid analysis technique to investigate the electronic and phonon structure of materials. The different symmetries involved govern whether vibrations are Raman active and appear in the spectra, whilst changes in lattice spacing and chemical environment shift band frequencies.

Raman spectroscopy is an effective method for studying material structure, so it is beneficial to use it to explore the surface layer structure of nanometer-sized crystals of cerium oxide, and to look for correlation between the change of the Raman spectrum of nanometer cerium oxide with

varying dopant size and dopant concentration. Till now, many temperature dependence measurements of the linewidths and frequency of the normal vibration of a crystal lattice have been carried out for crystals with various structures. However, very few experimental studies were carried to correlate between the changes of the Raman spectrum of nanometer cerium oxide as a function of dopant size. This study focuses on the change of the Raman spectrum with sizes of dopant in cerium oxide nanoparticles.

Cerium oxide has a cubic fluorite type structure and belongs to the $O_h^5 (Fm3m)$ space group. This structure has six optical-phonon branches, which yield three zone-center frequencies. These frequencies are 272, 465 and 595 cm^{-1} , corresponding to the doubly degenerated TO mode, the triply degenerate Raman-active mode and the nondegenerate LO mode, respectively. The triply degenerate Raman-active mode frequency can be directly detected by Raman measurements, whereas the TO and LO frequencies are given indirectly by fits to infrared reflectivity.

Raman spectra for the doped (20Sm, 40Sm, 20Gd, 40Gd, 20Y, 40Y, 20Yb and 40Yb) and undoped nanoceria synthesized by microemulsion method mentioned in sections in 2.4.1 and 2.4.2 were measured using a Horiba Jobin Yvon LabRam IR micro-Raman system with a spatial resolution of 2 micron. A helium-neon laser provided excitation at 633 nm with a power of 3mW. The Raman scattered light was collected by a 50x objective in a back-scattering geometry and dispersed with a single stage 800mm spectrograph equipped with a CCD detector. A 1200 grooves/mm grating and a pinhole size of 100 microns resulted in a spectral resolution of 2 cm^{-1} . A combination of Holographic notch and edge filters was used for Rayleigh line rejection.

In bulk, defect free crystalline materials, $q = 0$ phonons can be Raman active and observed. As the dimension and size of a material is reduced, an increasing volume of reciprocal space is sampled in Raman scattering. Several factors can contribute to the changes in Raman peak position and linewidth of 464 cm^{-1} peak with nanoparticle size. These include phonon confinement, strain, broadening associated with the size distribution, defects and variations in phonon relaxation with particle size.

Important information regarding the lattice disorder can be obtained from the analysis of the shape of the Raman line, which has been studied using the spatial correlation model. According to this model, the Raman line intensity, $I(\omega)$ at frequency ω can be written as:

$$I = \int_0^1 \exp\left(\frac{-q^2 L^2}{4}\right) \frac{d^3 q}{[\omega - \omega(q)]^2 + \left(\frac{\Gamma_0}{2}\right)^2} \quad (4)$$

where q is the wave vector expressed in units of $2\pi/a$ (a is the lattice constant). Γ_0 is the FWHM of Raman line of large grain sized material (6.9 cm^{-1} observed for microceria sample). The expression $\exp(-q^2 L^2/4)$ represents a Gaussian spatial correlation function with parameter L as correlation length and $\omega(q)$ is the function of Raman phonon dispersion.

For dispersion $\omega(q)$, we fitted the phonon dispersion determined from rigid-ion model⁹ with analytical model relations:

$$[w(q)]_1 = 506 - 44.105 \cos(\pi q) \quad (5)$$

$$[w(q)]_2 = 462.5 - 175 q^2 \quad (6)$$

$$[w(q)]_3 = 377.1 + 86.58 \cos(\pi q) \quad (7)$$

As the triple degeneracy of the Raman mode at 464 cm^{-1} is removed away from $q = 0$, equation (4) was summed over three equally weighted branches of the phonon dispersion given by equations (5), (6) and (7).

The Raman spectra line-shape fit was performed using the spatial correlation model explained above with only correlation length, L as a fitting parameter. The correlation length, L corresponds to the spheres with diameters equal to the distance between two next oxygen vacancies and can be used to determine the defect concentration, N as:

$$N = \frac{3}{4\pi L^3} \quad (8)$$

The oxygen vacancies concentration studied from the electrical conductivity measurements has been given as:

$$[V_{\ddot{O}}] = N_0 \exp\left(\frac{-\Delta H}{3kT}\right) \quad (9)$$

where $N_0 = 4.99 \times 10^{22} \text{ cm}^{-3}$ is the concentration of oxygen atoms in the Ceria lattice and ΔH denotes the changes in the enthalpy of oxygen vacancy formation. It was determined that ΔH changes with the grain size of cerium oxide Nanoparticles making the oxygen vacancies formation more favorable at smaller size.

Trivalent rare earth ions in the Ceria lattice deform the structure and can be detected by Raman analysis. Figure 3.2 (a) shows the measured Raman spectra for undoped and doped nanoceria samples. The peak frequencies for the single Raman line were determined by fitting the data to a Lorentzian line shape using PeakFit (Version 4.0) software. Figure 3.2 (b) show the Raman peak shift for all doped nanoceria samples with respect to undoped nanoceria, which indicates the shift of Raman peak towards lower energies for larger dopant size compare to Ce^{3+} and moves towards higher energies for smaller dopant size. This Raman shift can be explained by lattice distortion or lattice strain induced by the dopants as measured in XRD. With increasing dopant concentration the lineshape of the Raman-allowed mode gets progressively broader and asymmetric. The lattice disorder induced by the substitution of trivalent rare earth ions causes this shape change in the Raman line. The Raman spectra line-shape fit was performed using the spatial correlation model explained above with only correlation length, L as a fitting parameter. The correlation length was found to be decreasing with increasing (cation) dopant size and increasing with decreasing dopant size. The correlation length values for different dopants with 20 and 40 atom% were listed in the Table 3.1 and corresponding defect concentration for doped and undoped nanoceria were listed in the Table 3.2.

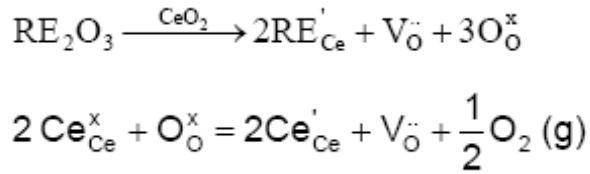
Table 3.1 Calculated correlation length (L) values for doped (Sm, Gd, Y and Yb) and undoped nanoceria

Dopant in Ceria (Atomic %)	Correlation Length (L)			
	Sm ³⁺ doped	Gd ³⁺ doped	Y ³⁺ doped	Yb ³⁺ doped
0	8.90	8.90	8.90	8.90
20	8.77	8.80	8.85	9.15
40	8.65	8.68	8.848	9.40

Table 3.2 Calculated Defect Concentration in doped (Sm, Gd, Y and Yb) and undoped nanoceria

Dopant in Ceria (Atomic %)	Defect Concentration			
	Sm ³⁺ doped	Gd ³⁺ doped	Y ³⁺ doped	Yb ³⁺ doped
0	3.39E+20	3.39E+20	3.39E+20	3.39E+20
20	3.54E+20	3.5E+20	3.45E+20	3.12E+20
40	3.69E+20	3.65E+20	3.45E+20	2.88E+20

Figure 3.3 (a) shows the determined correlation length for doped nanoceria as a function of doping concentration. Figure 3.3 (b) presents the defect concentration calculated from the correlation length as given in equation (8). The defect concentration gradually increases with dopant concentration. When Ce^{4+} ions are substituted by RE^{3+} ions, the oxygen vacancies are introduced into the fluorite lattice by partial reduction of Ce^{4+} to Ce^{3+} so as to maintain the electric neutrality. This reduction process can be given as follows:



where RE = Sm or Gd or Y or Yb.

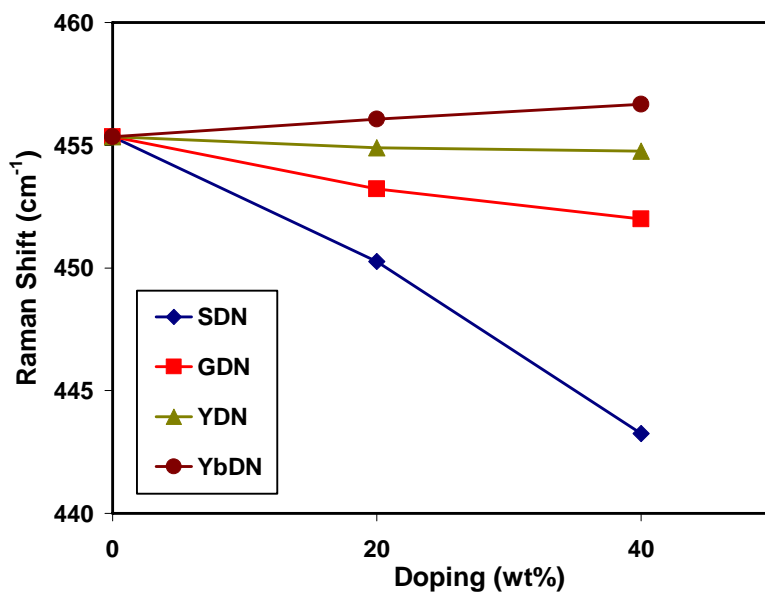
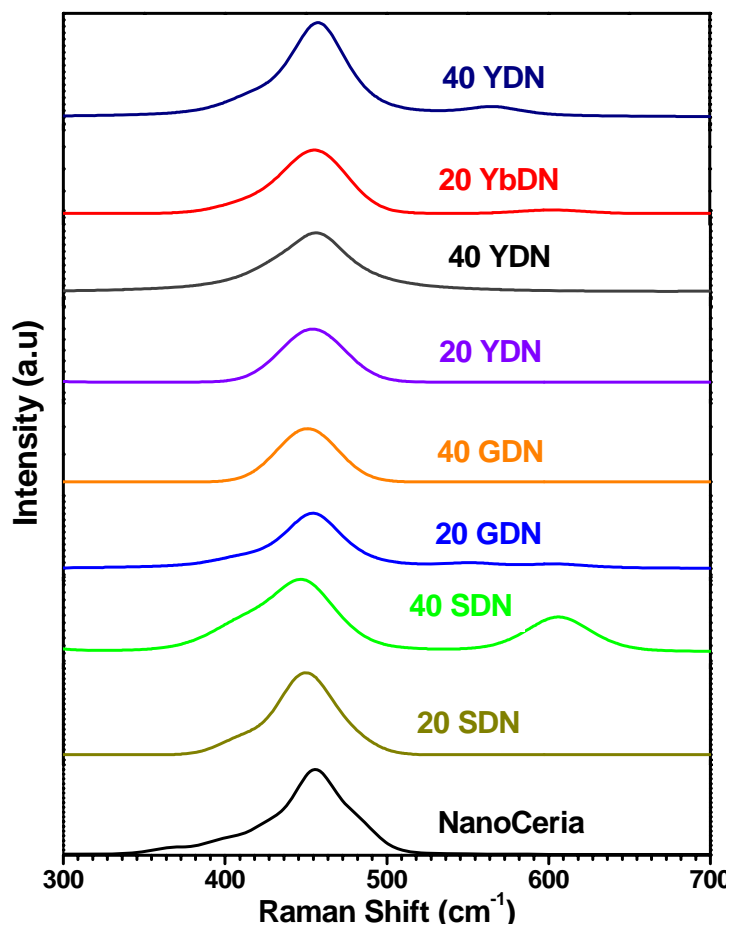


Figure 3.2 (a) Raman spectra of undoped and doped (Sm, Gd, Y and Yb) nanoceria samples (b) Raman peak shift of the nanoceria samples as a function of doping amount.

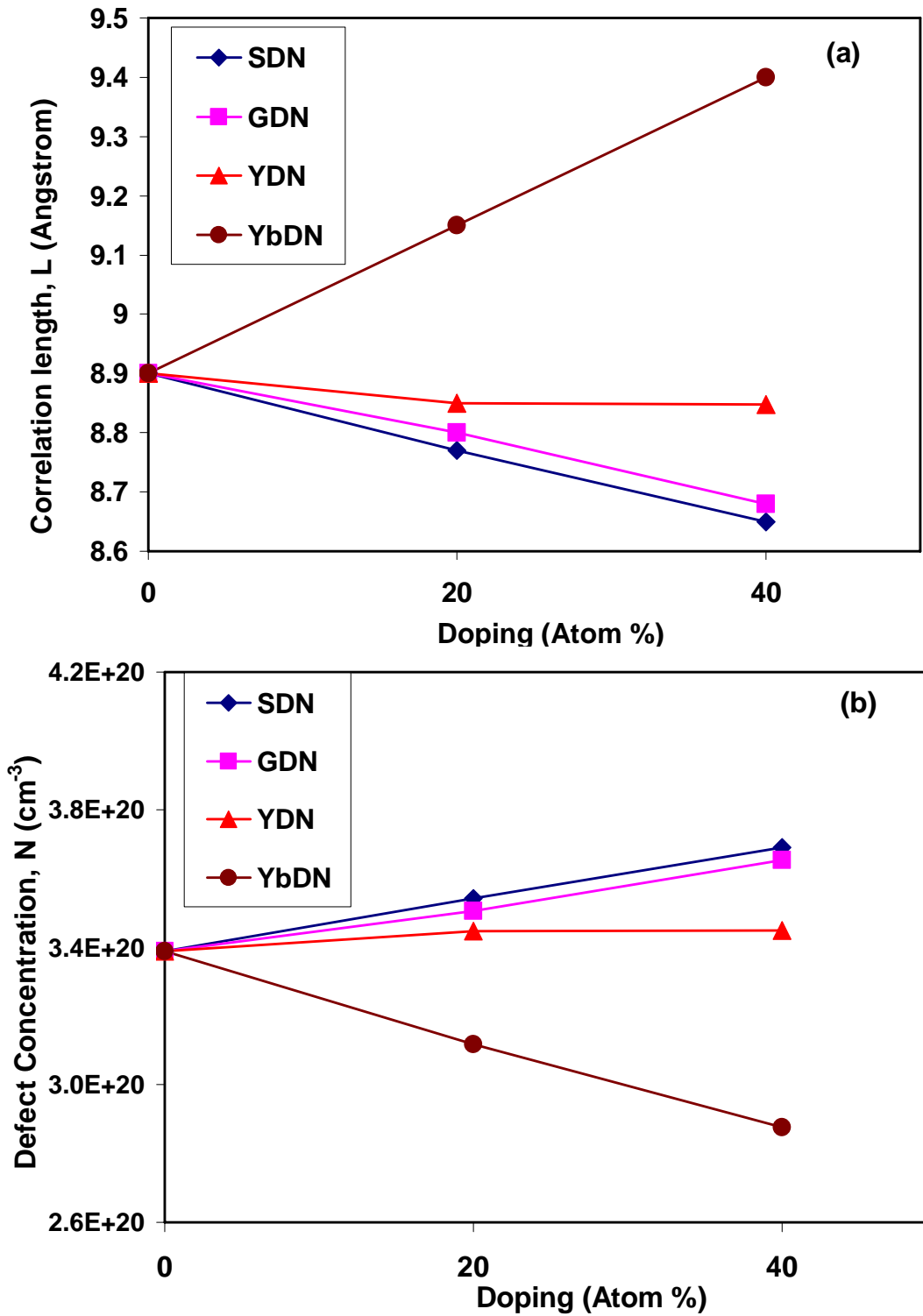


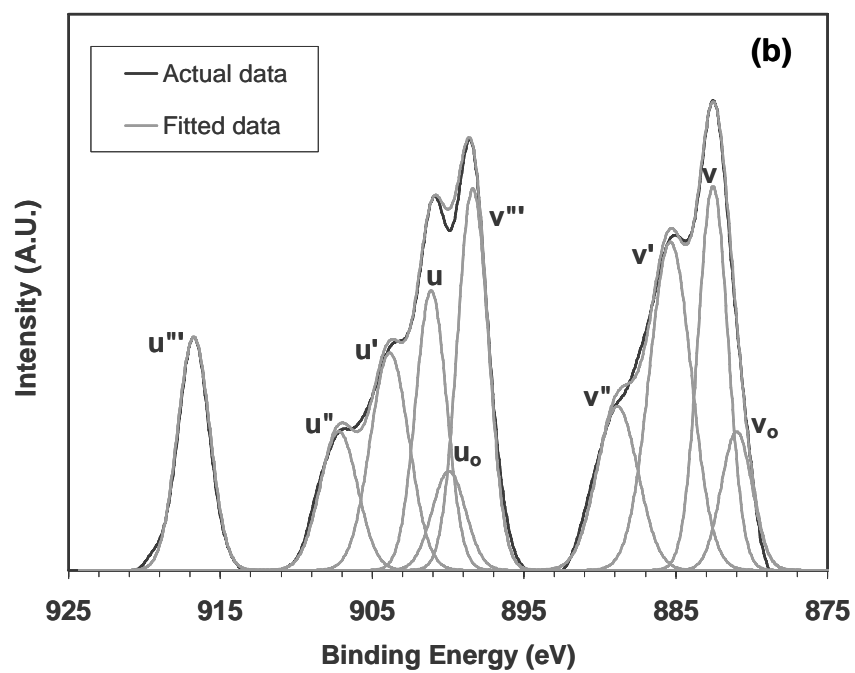
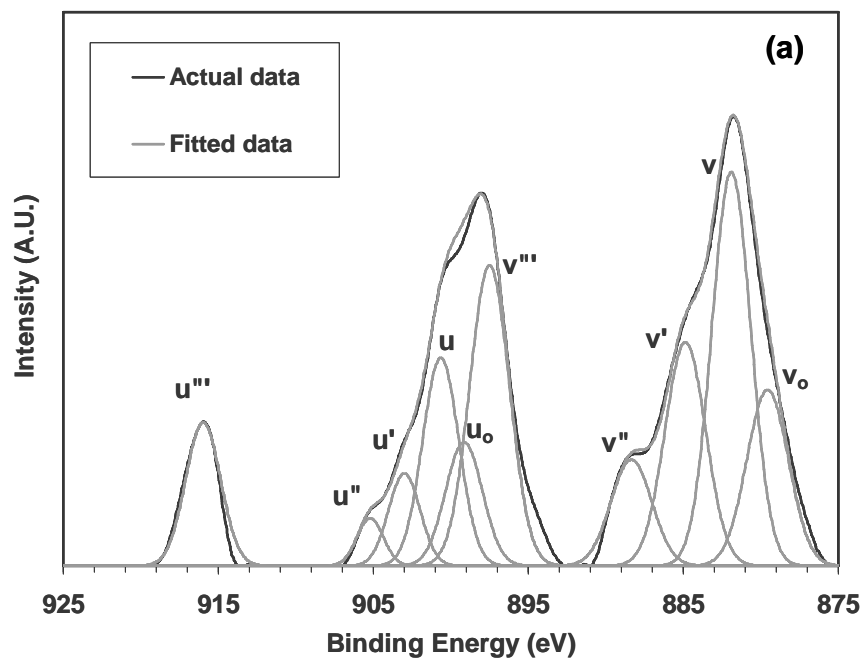
Figure 3.3 (a) The correlation length and (b) Oxygen vacancies Concentration of the nanoceria samples as a function of doping amount.

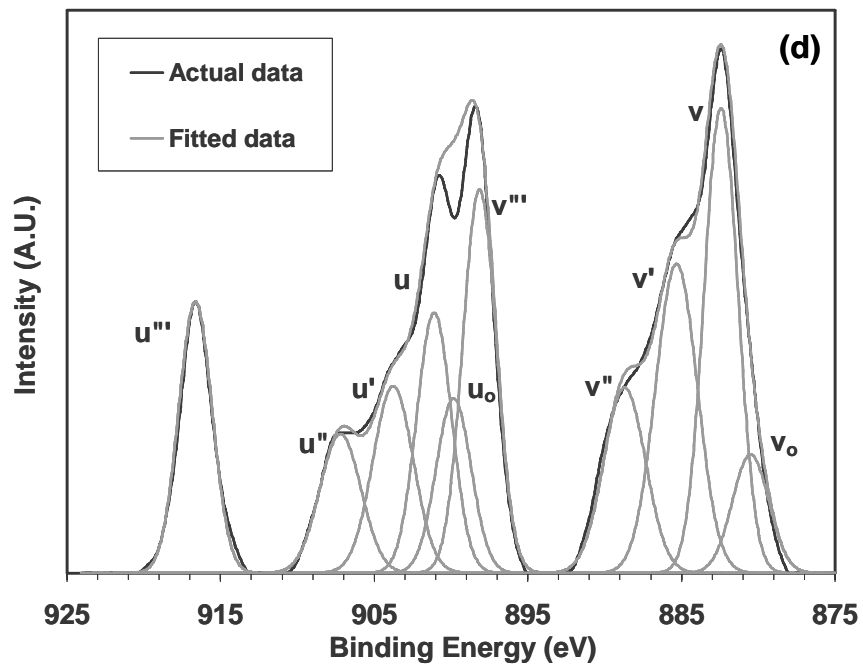
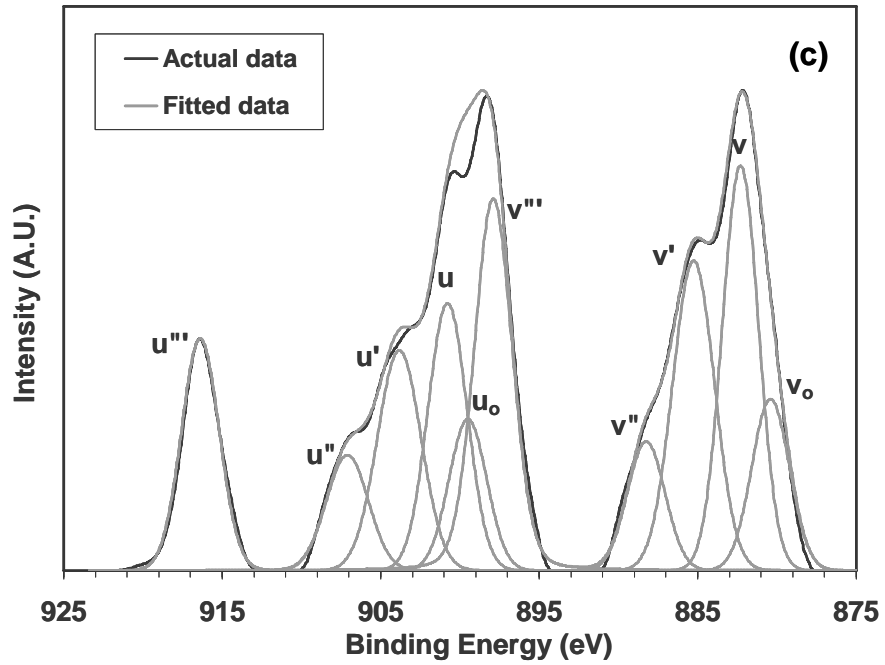
3.2.3 X-Ray Photoelectron Spectroscopy Analysis

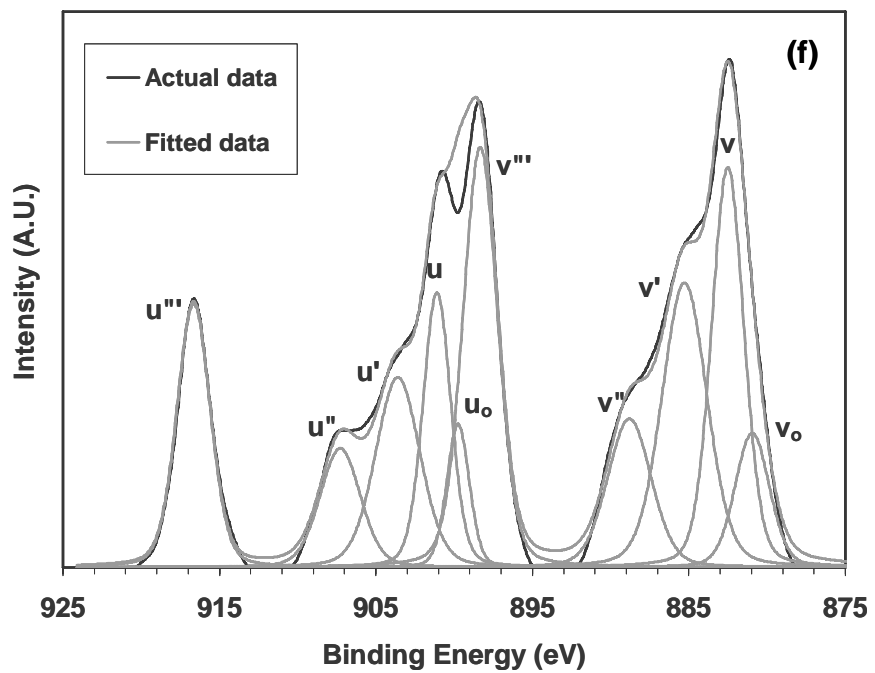
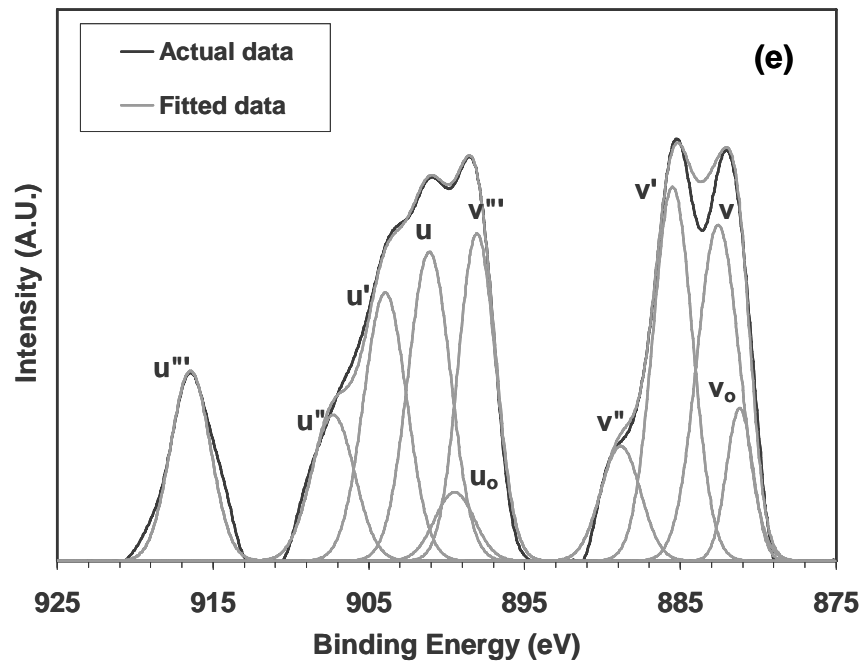
X-ray Photoelectron Spectroscopic (XPS) (PE-PHI5400) analysis was carried out on NC, 20 GDN, 40 GDN, 20 YDN, 40 YDN, 20 YbDN and 40 YbDN samples in order to study the changes in the nanoceria surface valence chemistry. The peak positions and FWHM for all cerium peaks were fitted using PeakFit (Version 4.0) software for all undoped and doped nanoceria samples¹⁰. Figure 3.4 shows the deconvoluted XPS Ce (3d) spectrum for undoped and doped nanoceria samples. In this, v_o , v' , u_o and u' peaks are the characteristic peaks of Ce^{3+} ; while v , v' , v'' , u , u'' and u''' are attributed to Ce^{4+} ions. Similar peak fitting was also done for XPS spectra of NC, 20 GDN, 40 GDN, 20 YDN, 40 YDN, 20 YbDN and 40 YbDN samples and peak positions were listed in the Table 3.3. A semiquantitative analysis of the integrated peak area can provide the concentration of Ce^{3+} ions in the undoped and doped nanoceria particles. It can be calculated as:¹¹

$$[Ce^{3+}] = \frac{A_{v_o} + A_{v'} + A_{u_o} + A_{u'}}{A_{v_o} + A_{v'} + A_{u_o} + A_{u'} + A_v + A_{v''} + A_{v'''} + A_u + A_{u''} + A_{u'''}} \quad (10)$$

Where A_i is the integrated area of peak 'i'.







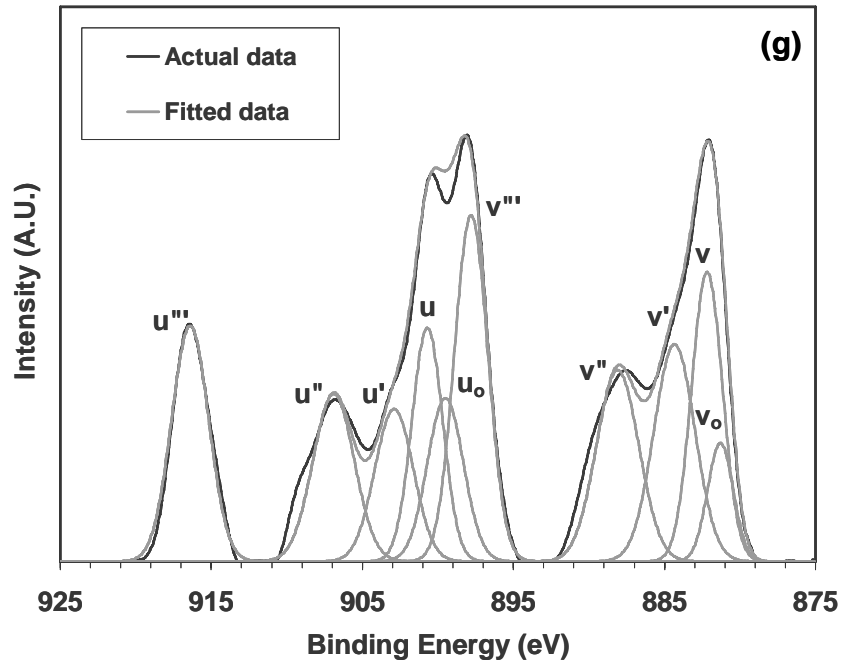


Figure 3.4 Peak fitted XPS spectrum of Ce (3d) for (a) Nanoceria (b) 20 GDN (c) 40 GDN (d) 20 YDN (e) 40 YDN (f) 20 YbDN (g) 40 YbDN

Table 3.3 XPS binding energies of individual peaks of the Ce(3d) spectrum for undoped and doped nanoceria

Samples	Ce (3d _{5/2})					Ce (3d _{3/2})				
	V_0	v	v'	v''	v'''	u_0	u	u'	u''	u'''
NC	879.56	881.90	884.87	888.35	897.50	899.15	900.65	903.00	905.20	915.98
20GDN	880.99	882.50	885.36	888.85	898.37	899.95	901.12	903.85	907.20	916.76
20YDN	880.50	882.42	885.33	888.70	898.15	899.83	901.10	903.77	907.20	916.64
20YbDN	880.95	882.51	885.28	888.80	898.33	899.75	901.10	903.60	907.28	916.65
40GDN	880.40	882.30	885.26	888.25	897.90	899.50	900.78	903.83	907.10	916.38
40YDN	881.20	882.58	885.50	888.84	898.06	899.50	901.12	903.95	907.30	916.45
40YbDN	881.30	882.18	884.34	888.10	897.80	899.50	900.70	902.90	906.90	916.40

Figure 3.5 shows the ratio of Ce^{3+} to Ce^{4+} concentration in undoped and doped nanoceria (20 GDN, 40 GDN, 20 YDN, 40 YDN, 20 YbDN and 40 YbDN) samples. It shows that the concentration of Ce^{3+} increases with increase in dopant concentration for Gd and Y while Ce^{3+} concentration decreases with increase in concentration for Yb. This can be attributed to the increase in the lattice parameter (as well as oxygen vacancy concentration) by doping larger ions (Gd^{3+} , Y^{3+}) where as decrease in lattice parameter (as well as oxygen vacancy concentration) by doping smaller ions (Yb^{3+}).

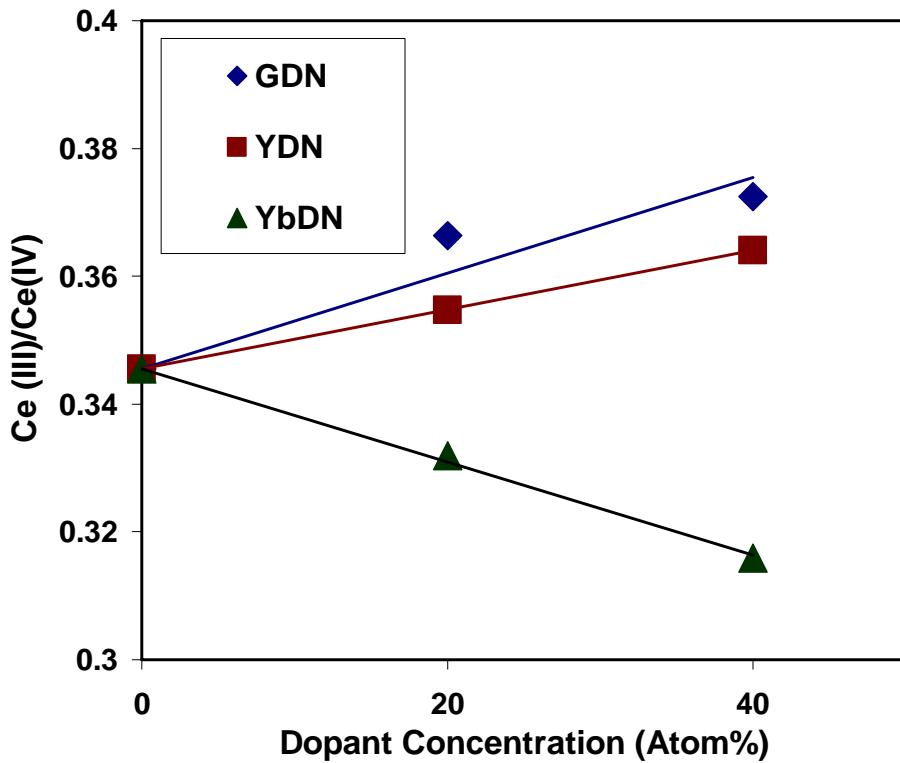


Figure 3.5 Concentration ratio of Ce^{3+} to Ce^{4+} as a function of dopant concentration for dopants Gd, Y and Yb as calculated using equation 10.

3.3 Conclusion

Cerium oxide nanoparticles show lattice strain by introducing trivalent dopants into ceria fluorite crystal lattice. XRD analysis of doped nanoceria indicates lattice expansion in case of larger trivalent dopants (Gd^{3+} , Y^{3+}) and lattice contraction in smaller dopants (Yb^{3+}). It also shows that the change in lattice parameter in nanocrystalline cerium oxide doping larger or smaller dopants is approximately proportional to ionic size of the trivalent rare earths.

Raman spectra of doped nanocrystalline cerium oxide also showed broadening of Raman peak in doped nanoceria particles. It also showed shifting of Raman peak to lower energies for Sm, Gd, and Y-dopings and to higher energies for Yb-dopings in nanoceria; similar to XRD results where larger trivalent ions increases lattice parameter and smaller ions decreases lattice parameter of nanocrystalline ceria. Spatial correlation model was developed for cerium oxide and used to fit the experimental Raman spectra using the correlation length, L as the only fitting parameter. The analysis indicated that the lattice parameter variation observed in cerium oxide nanoparticles as a function of dopant concentration is due to the formation oxygen vacancies in the ceria lattice by doping larger or smaller trivalent ions. In case of doping with trivalent elements, the oxygen vacancies are formed to maintain the electric neutrality.

X-ray Photoelectron Spectroscopy analysis on the undoped and doped nanoceria particle showed that there is an increase in Ce^{3+} ions in nanoceria doped with larger dopants (Gd and Y) and the increase in Ce^{3+} ion concentration is proportional to dopant concentration. It also showed that there is a decrease in Ce^{3+} ion concentration by doping with Yb^{3+} (smaller compare to Ce^{3+}) and this decrease is proportional to Yb concentration in nanoceria.

From XRD, Raman and XPS analyses of undoped and doped nanoceria particles synthesized by microemulsion method, there is a variation of lattice parameter by doping with larger or smaller trivalent ions in nanoceria. Oxygen vacancies are created in doped and undoped nanoceria to maintain charge neutrality in presence of trivalent ions. This lattice parameter change is because of the difference in the oxygen vacancy concentration (Raman analysis) caused by the dopant size variation as all the undoped and doped nanoceria particles are of 3-5 nm size as shown in TEM micrographs of particles. It indicates that Ce^{3+} concentration variation in doped nanoceria particles is because of lattice expansion or contraction created by doping larger (Gd^{3+} and Y^{3+}) or smaller ions (Yb^{3+}). The above study helps in altering the nanocrystalline cerium oxide properties by doping different trivalent dopants and formation of non-stoichiometric cerium oxide nanoparticles which are useful in various applications.

CHAPTER 4. APPLICATION OF DOPED AND UNDOPED NANOCERIA IN HIGH TEMPERATURE OXIDATION PROTECTION

4.1 Introduction

Many high temperature alloys rely on the formation of protective Al_2O_3 and Cr_2O_3 scales on their surface to resist high temperature oxidation¹²⁻¹⁵. However, under various isothermal and thermal cycling conditions, these protective coatings crack due to thermal stresses and grain growth. Oxide scale cracking and spalling restrict the application of such alloys as high temperature oxidation resistant materials under demanding service conditions¹³. This spalling may be induced by stresses arising from the oxide growth process itself, strains resulting from mechanical flexing of the component in service, or from stresses arising from thermal cycling because of the difference in the coefficients of thermal expansion of the oxide and the metal. Spallation of oxide may involve fracture in the oxide adjacent to the metal surface, fracture in the metal immediately below the interface, or by separation at the interface itself.

Approximately fifty years ago, it was discovered that minor amounts of reactive elements, added as a cerium mischmetal deoxidizer to the melt prior to the development of vacuum melting, had a profound effect on the lifetime of heater alloys. The extreme chemical affinity of the rare earth elements for almost anything that they may contact suggests that they will also interact strongly with inclusions in most metals, but little is known about the mechanism by which this occurs.

A more recent discovery suggests that small additions of the lanthanides may confer even greater protection on those metals and alloys that are already well protected from corrosion by oxide films. These include the iron-chromium and iron-chromium-nickel stainless steels (i.e., both the ferritic and austenitic alloys), and most other alloys that are dependent on chromium for their corrosion/oxidation resistance. Further study may suggest that the effect is even broader - e.g., that the protection provided by all spinel-forming oxides such as Al_2O_3 or Cr_2O_3 is enhanced in this way. Use of rare earths as alloying additions for corrosion control shows promise of becoming a major growth market. There is also strong evidence that at least cerium acts as a grain-refining agent in some steel compositions, just as it apparently does for aluminum and magnesium alloys, with corresponding improvements in mechanical properties and fatigue resistance.

Addition of rare earth elements such as Ce, Y, Zr, La or their oxides improve the high temperature oxidation resistance of the alumina and chromia forming alloys due to the reactive-element effect (REE) ¹⁶⁻²¹. Due to REE the oxide scale growth rate decreases with an improvement in resistance to scale spalling by increasing the scale–alloy adhesion.

In spite of the commercial importance of the effect, and recognized for long time, a generally accepted theory does not exist. Various researchers have put forward several mechanisms to explain the REE. Antill & Peakall ¹² indicated that the beneficial effect of the rare earth elements was primarily to improve the scale plasticity for accommodating stresses due to the difference in the thermal expansion coefficients between the alloy and the oxide scale. The enhancement of oxide nucleation processes through the presence of rare earth elements was suggested by Stringer ¹⁴. Tien & Pettit ¹⁵ reported that the application of rare earth elements provide sites for vacancy

condensation in a Fe–25Cr–4Al alloy to improve of scale adhesion. The mechanism of pegging the oxide scale to the alloy substrate was also suggested by others²². Duffy & Tasker²³ supported the model of grain boundary blocking by Ce⁴⁺ ions, which associate with metal vacancies to form arrays of defect pairs along the grain boundaries.

Application of the reactive-element coating on the metals and alloys to improve their high-temperature-oxidation resistance is more advantageous than the presence of the rare earth in the form of alloy constituents that usually pose difficulty in alloy processing especially during hot working. Researchers²⁴ have suggested that the surface deposition of the reactive-element oxide in the case of chromia-forming alloys can harness the beneficial effect of REE. Moon & Bennett²⁵ concluded that the scale nucleates at the reactive-element oxide particles on the surface, blocks short-circuit diffusion paths by segregating reactive-element ions, and reduces the stresses in the oxide scale by altering the microstructure.

4.2 Literature Review

Cerium oxide (Ceria) based materials have been extensively studied and used in various applications over the past two decades, including enhancement of high-temperature-oxidation resistance of metals and alloys. Nanoceria (NC) has been shown to possess unique properties from its large scale complement such as the shifting and broadening of Raman-allowed modes²⁶ lattice expansion^{27, 28} and blue shift in ultraviolet absorption spectra²⁹. As a result of unique properties NC has potential applications in UV protection, catalysis³⁰⁻³⁴, and high temperature oxidation resistance. Recently, it has been reported that small additions of lanthanides may confer even greater protection on those metals and alloys that are already well protected from

corrosion by oxide films¹³. These include iron-chromium and iron-chromium-nickel stainless steels (i.e., both ferritic and austenitic alloys), and most other alloys that are dependent on chromium for their corrosion/oxidation resistance.

It was first reported that ceria could be superficially applied rather than as an alloy addition and chromia growth could be slowed down³⁵. Earlier studies^{24, 36} have indicated that superficial coating of micrometer-sized cerium oxide particles is effective in improving the high temperature oxidation resistance of various grades of stainless steels. However, it was not effective in protecting AISI 304 grade stainless steel from high-temperature oxidation in dry air¹⁶. Nanoparticles of ceria are expected to improve the oxidation resistance of chromia- and alumina forming alloys because of their easy dissolution in the grain boundaries and subsequent blocking of short-circuit diffusion paths more effectively compared with that of the micrometre-sized ceria particles. Preliminary investigations on the improvement of high temperature oxidation resistance of Ni, Cr and Ni–Cr super alloys with the application of NC coating were carried out by various researchers^{3, 37}. It was also reported that NC coating improve high temperature oxidation resistance of chromia forming steels³⁸. However, detailed investigations on the effect of undoped and doped ceria nanoparticles and the role of oxygen vacancies for the improvement of high temperature oxidation resistance of SS are yet to be carried out.

4.3 Experimental Procedure

AISI 304 grade SS samples with a thickness of 3 mm were used in the present study. The chemical composition (wt %) of the SS samples used in the present study is as follows: C, 0.05; Mn, 1.45; Si, 0.51; Cr, 17.9; Ni, 8.85; S, 0.015; P, 0.029; and Fe, the balance. The SS substrates

used were about 12.5mm x 12.5mm with a small hole of 1/16 inch drilled near an edge so as to hang the sample in the thermobalance. Specimens were polished by 1200 grit SiC polishing paper and cleaned ultrasonically in ethanol. It was reported that pre-oxidation of the substrate improves the surface wetting and forms a thin, adherent oxide layer on the alloy surface ³⁹. Hence, the polished, cleaned SS specimens were pre-oxidized at 973 K for 2 min in dry air, followed by cooling in air. The weight gain of the specimen due to such pre-oxidation treatment was found to be less than 0.01 mg.

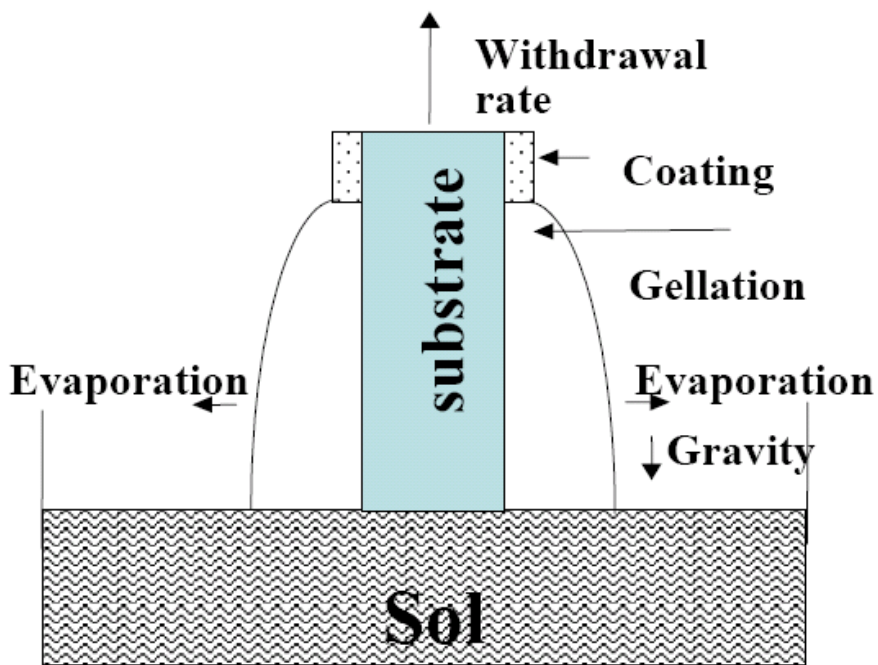


Figure 4.1 Dip Coating Process used for coating doped and undoped ceria on AISI 304 SS samples

The pre-oxidized samples were dip coated in doped and undoped ceria solutions as shown in the Figure 4.1. Triton-X 100 was added to doped and undoped ceria solutions (5ml to 45ml of solution) in order to increase the adhesion of the particles to the pre-oxidized SS surface. The samples were coated in 12 steps in nanocrystalline solutions synthesized by microemulsion

method. In each step the sample was dipcoated 5 times in the solution at 68.55mm/min. After each step the sample was dried at 200⁰C for 15 min. For equivalent coating, the same coating weight of $2 \times 10^{-3} \text{ g cm}^{-2}$ was used for all the specimens with a coating thickness of 600nm.

SS substrate as well as MC, NC and Lanthanum doped nanoceria (LDN) coated samples were oxidized at 1243 K for 24 h in dry air. The oxidation kinetics were measured continuously in a thermogravimetric set-up consisting of a microbalance (Sartorius, model LA230P, $\pm 0.01 \text{ mg}$), a vertical furnace with temperature-controlling accessories, and a computer for continuous data acquisition. The details of the high temperature oxidation set-up used in the present study are described elsewhere^{24, 40}. Scale morphology of the oxidized samples coated with NC and 2, 20 and 40 LDN was studied using a JEOL T-300 SEM with an acceleration voltage of 5 kV. The elemental analysis of the oxide scale formed on the NC and 20 LDN samples was carried out using the energy dispersive spectroscopy (EDS). Cross sectional SEM studies were carried out for NC and 20 LDN samples. Both line profile and x-ray elemental scanning was done for elemental analysis across the oxide layer. XRD analyses of top oxide layer on uncoated, NC and 20 LDN samples were carried out using Rigaku Analytical Diffractometer with Cu K_α radiation ($\lambda = 0.154056 \text{ nm}$). SIMS depth-profile analysis was carried to map the distribution of the elements in the oxide scale formed on NC, 20 LDN samples, using the ADEPT 1010 system from Physical Electronics Inc. It consisted of an ion gun operated with 3 keV cesium beam at 60⁰ to the specimen normal. The beam was rastered over a $250 \mu\text{m} \times 250 \mu\text{m}$ square area. The analysis was carried out from the signal coming from the central 30% of the sputter crater area.

4.3.1 Sample Preparation for SEM analysis

4.3.1.1 Sample Preparation for Top Surface Analysis

In order to remove the charging effect of samples in SEM, NC, and LDN coated and oxidized SS samples were sputter coated with Au/Pd for 2 minutes in the sputter coater. These samples were kept in the vacuum for a day before analyzing the top surface under SEM.

4.3.1.2 Sample Preparation for Cross Sectional Analysis

Both NC and 20 LDN coated and oxidized samples were cut using a diamond cutter across the sample. These samples were kept in reusable rubber mounting cups with cross-sectional surface facing towards bottom of cup which coated with mold release first for easy removal after curing. The mounting cup is filled with 100 parts low viscosity epoxy resin (Epo-thin[®]) to 39 parts low viscosity epoxy hardner (Epo-thin[®]) and has been cured at room temperature for 24h. The sample was taken out from mounting cup for further polishing purpose. The sample was polished on Stuart Labopol-2 with 250 rpm speed. The polishing procedure of the samples was done in the following steps.

The sample was polished on (i) two SiC 120 grit polishing papers for 1 min each.(ii) two SiC 220 grit polishing papers for 1 min each (iii) MD Piano 220 polishing cloth which is covered with 9 μm suspension and lubricant for 1 min (iv) MD Largo which is covered with 6 μm suspension and lubricant for 1 min (v) MD Dac which is covered with 1 μm suspension and lubricant for 5 min (vi) MD Chem which is covered with Silica suspension in water for 1 min.

The sample was cleaned with acetone after all the above steps and sputter coated with Au/Pd for 2 min in sputter coater in order to remove charging effect that occurs while analyzing in SEM. These samples were kept in the vacuum for a day before analyzing the top surface under SEM.

4.4 Results and Discussion

4.4.1 Oxidation Kinetics

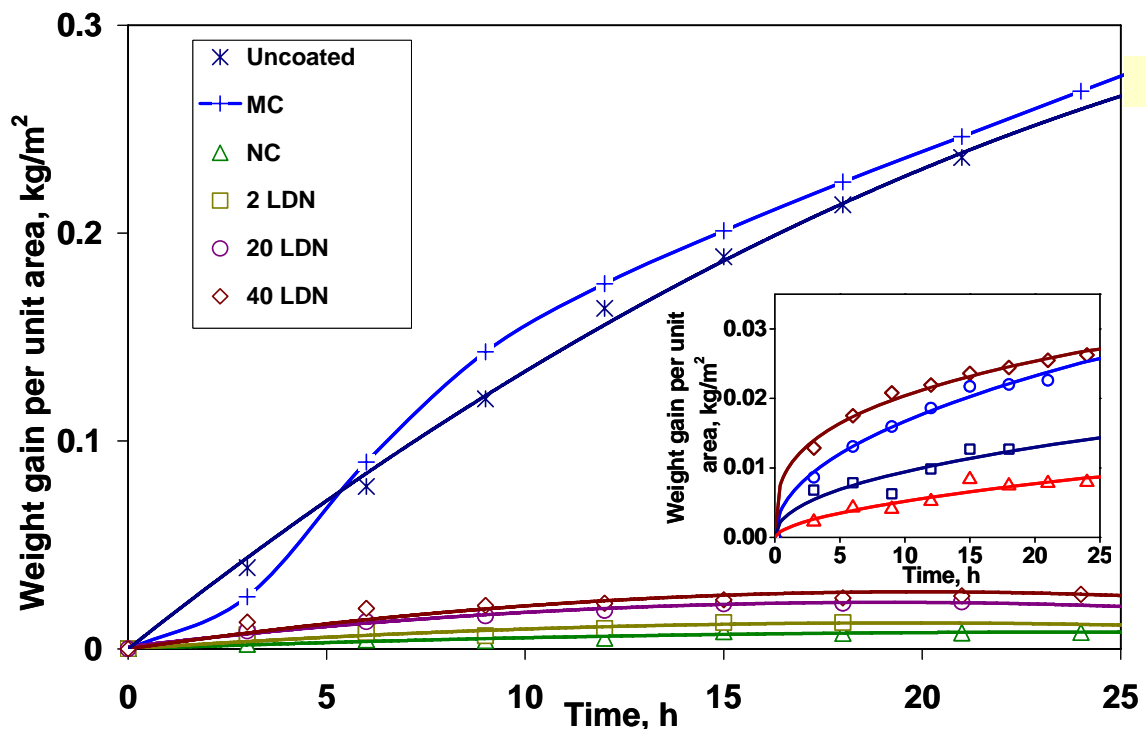


Figure 4.2 Weight gain per unit area versus time plots for isothermal oxidation of AISI 304 SS at 1243 K in dry air for 24h.

The oxidation kinetic plots of SS, MC, NC, 2 LDN, 20 LDN and 40 LDN coated AISI 304 grade SS samples at 1243 K in dry air for 24 h are shown in Figure 4.2. The NC coated sample showed improvement in the high temperature oxidation resistance over the uncoated and MC coated

samples. During the initial stages of oxidation in the bare alloy, Cr₂O₃ layer forms on the top surface. After the formation of Cr₂O₃ as the top layer, subsequent oxidation is by slow diffusion of other alloy elements through the Cr₂O₃ layer leading to reduced rate of oxide scale growth in the later stages, but the protective chromia layer fails due to stresses and thermal-expansion-coefficient mismatch between the oxide scale and the substrate. This is observed in the uncoated and MC coated samples, where a steady weight gain is observed. Moreover, the chromia layer is prone to evaporation at high temperature as CrO₃ species⁴¹. However, when coated with LDN the weight gain is slightly increased as compared to the NC coated sample as shown in the Figure 4.2. (Inset figure). It also showed that the weight gain per unit area increases with dopant concentration in the initial stages, however, the oxide scale is still protective following the parabolic growth law kinetics. This indicates that large amounts of dopant concentration reduces the oxidation resistance compared to NC but provides better protection than that of SS and the MC sample. The thermogravimetric analysis showed a parabolic relationship with kinetics as shown in the equation.

$$\frac{dw}{dt} = \frac{k_p}{2w} \tag{11}$$

Where w is the weight gain per unit area of the sample (g/cm²), and k_p is the parabolic oxidation rate constant (g²/cm⁴s). Such a parabolic law introduces the fact that the oxide growth is controlled by diffusion⁴². The k_p values are reported in Table 4.1. The obtained k_p values are representative of Cr₂O₃ healing layer formation⁴³. The k_p values are reduced four orders of

magnitude in the case of NC coating and the reduction is 2-3 orders of magnitude for LDN coatings compared to uncoated and MC sample.

Table 4.1 Parabolic rate constants or K_p values for oxidation of bare and pure and doped ceria-coated AISI 304 stainless steel samples at 1243 k for 24h

Sample	k_p values ($\text{kg}^2 \text{m}^{-4} \text{s}^{-1}$)
Uncoated	$1.50 \pm 0.01 \times 10^{-03}$
MC	$1.80 \pm 0.02 \times 10^{-03}$
NC	$6.25 \pm 0.05 \times 10^{-07}$
2 LDN	$6.40 \pm 0.05 \times 10^{-06}$
20 LDN	$2.00 \pm 0.02 \times 10^{-05}$
40 LDN	$2.26 \pm 0.02 \times 10^{-05}$

The observed weight gain for the NC and doped ceria coated samples in the initial exposure is due to the oxygen inward diffusion filling the oxygen vacancies created in the coatings⁴⁴. At the same time, the initial protective chromia layer forms, the thickness of the oxide layer increasing with increasing oxygen availability. After the initial exposure, the weight gain in NC and LDN

samples remains constant, showing the protective nature of the coating. It showed that both doped and undoped ceria coated SS samples can be protected from high temperature oxidation. Upon high temperature oxidation, NC particles in the coating provide extra nucleation sites for chromia formation. Consequently, the surface below NC coatings is completely covered by chromia more rapidly³⁸. Therefore, the early formation of protective chromia becomes more favored as the number of ceria particles on the surface is increased. Hence, it would enable NC coating to provide faster and earlier formation of the chromia healing layer on the surface.

4.4.2 Morphological Studies

4.4.2.1 Top Surface Morphology

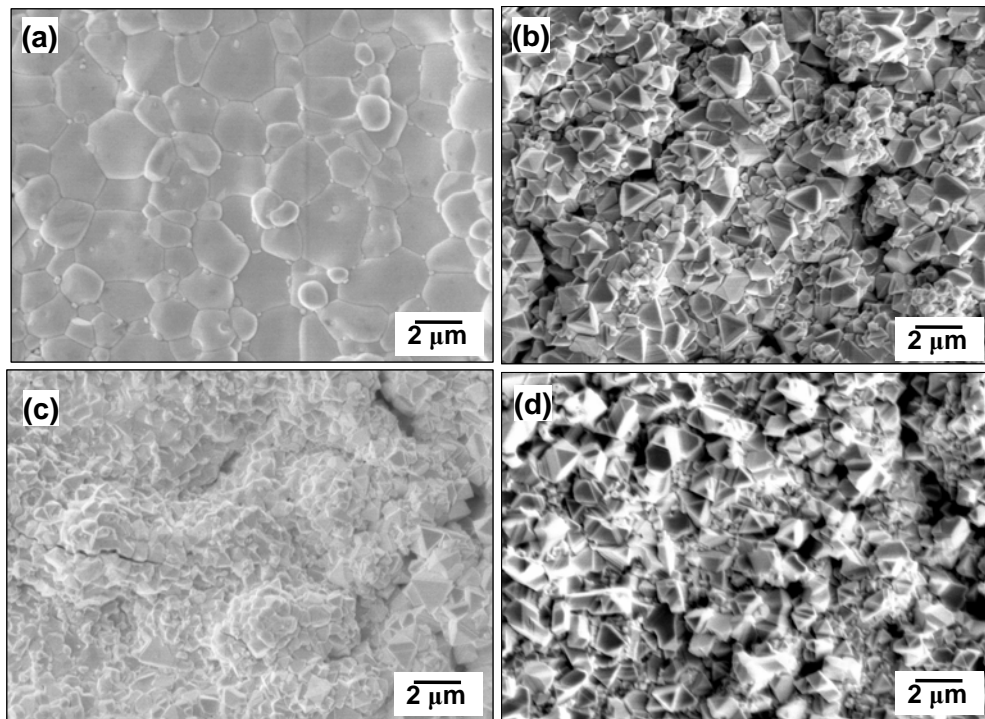


Figure 4.3 SEM micrographs of top oxide scale formed on the (a) NC, (b) 2 LDN, (c) 20 LDN and (d) 40 LDN SS at 1243K (at 5000X).

The oxide scale formed on NC sample is compact; whereas all LDN samples have a relatively faceted and porous structure as shown in Figure 4.3. The amount of doping increases the nucleation sites and forms a fine grain oxide layer on the surface. The fine-grained oxide layer formation in the case of LDN samples is due to the heterogeneous nucleation³⁶ caused by the presence of defects in the coating as shown in Figure 4.3. The formation of fine grained chromium oxide⁴⁵ on the surface of LDN samples shows that the diffusion of iron is restricted by segregation of doped ceria nanoparticles. The segregation of ceria at the grain boundaries, which is also prevalent in the doped ceria coated sample, prevents the outward diffusion of chromium but enhances inward oxygen diffusion. This is observed in Figure 4.2, where weight gain per unit area is reduced by more than 90% for NC and LDN samples as compare to uncoated and MC coated samples for isothermal oxidation at 1243 K in dry air for 24h. There is a marked improvement in the spalling resistance under isothermal oxidation conditions observed in both NC and LDN samples.

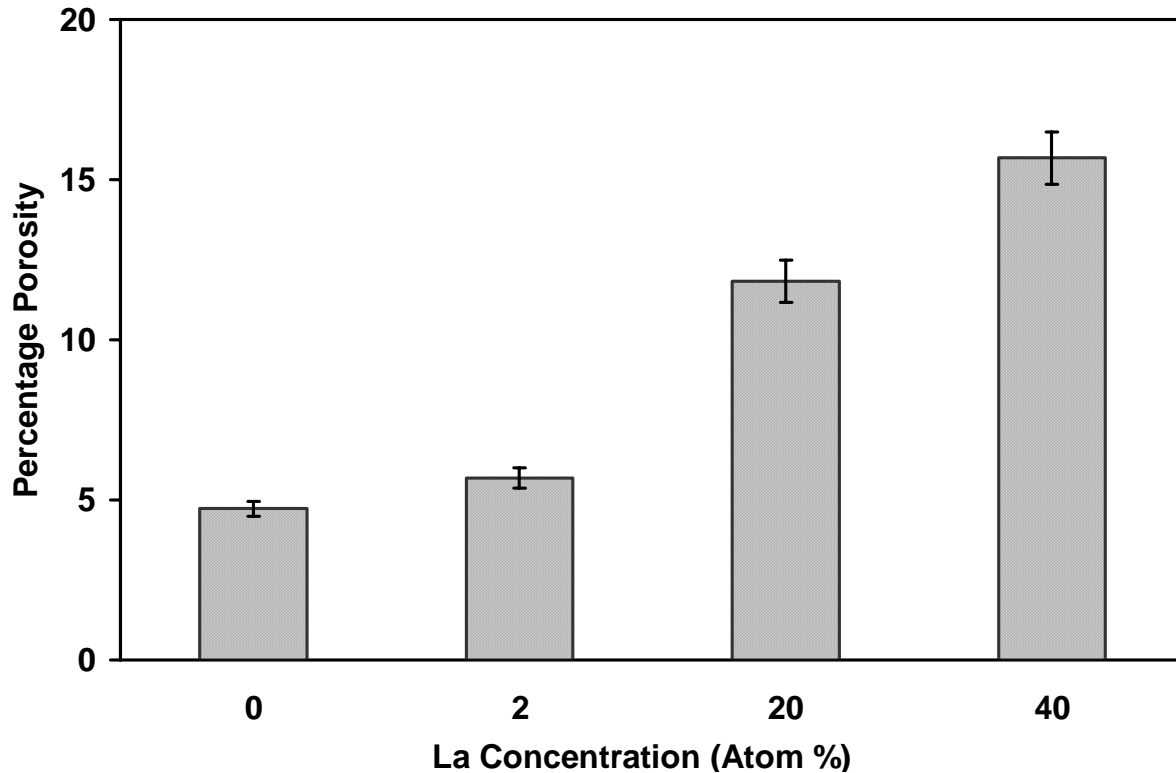


Figure 4.4 The average percentage porosity on the top oxide layer formed on AISI 304 stainless steel coated with NC and 2, 20 and 40 LDN and oxidized at 1243 K for 24 h in dry air.

The average porosity of oxide scale formed on NC, 2 LDN, 20 LDN and 40 LDN samples is 4.72 ± 0.24 %, 5.68 ± 0.32 %, 11.84 ± 0.66 % and 15.68 ± 0.82 %, respectively as shown in Figure 4.4. Increasing the dopant concentration in NC coatings led to high porosity in the oxide scale formed on the steel sample.

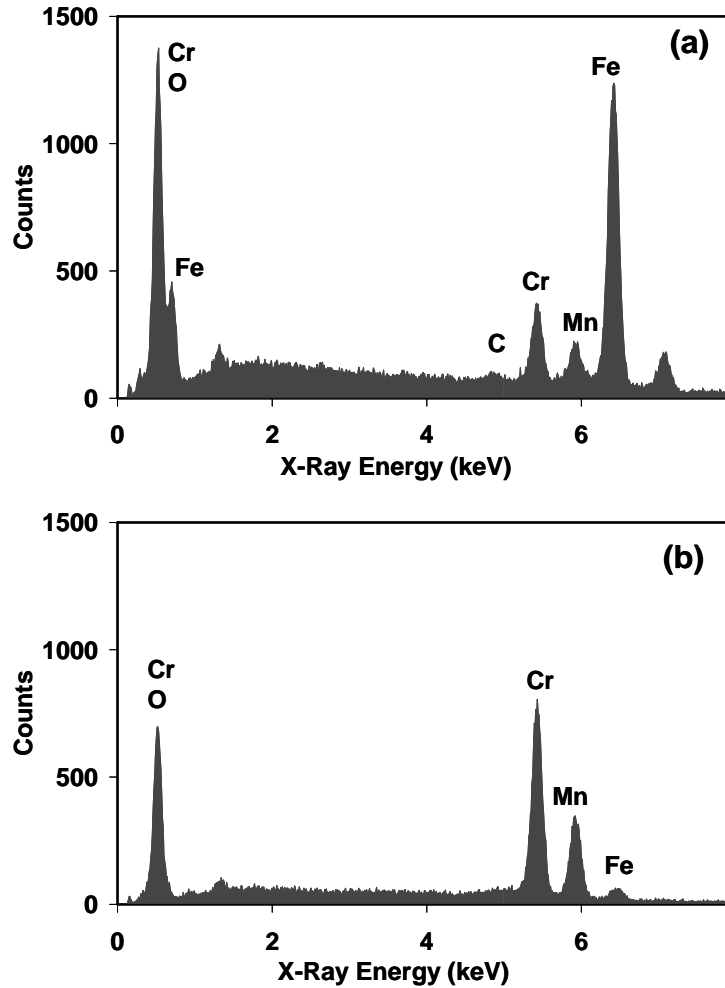


Figure 4.5 EDX spectra of the top oxide scale formed on NC (top) and 20 LDN (bottom) coated SS at 1243 K.

The EDX spectra of the top oxide scale of 20 LDN sample showed more amount of chromium on the surface oxide layer than that of NC sample as shown in Figure 4.5. The increase in chromium is due to enhancement of chromium oxide formation assisted by the inward oxygen diffusion. It also indicates a relatively thicker oxide scale in LDN sample. The fine grain structure is clearly seen in the case of LDN samples which increase the grain boundary area for diffusion of Fe, Cr through the initial healing chromia layer.

4.4.2.2 Cross Section Morphology

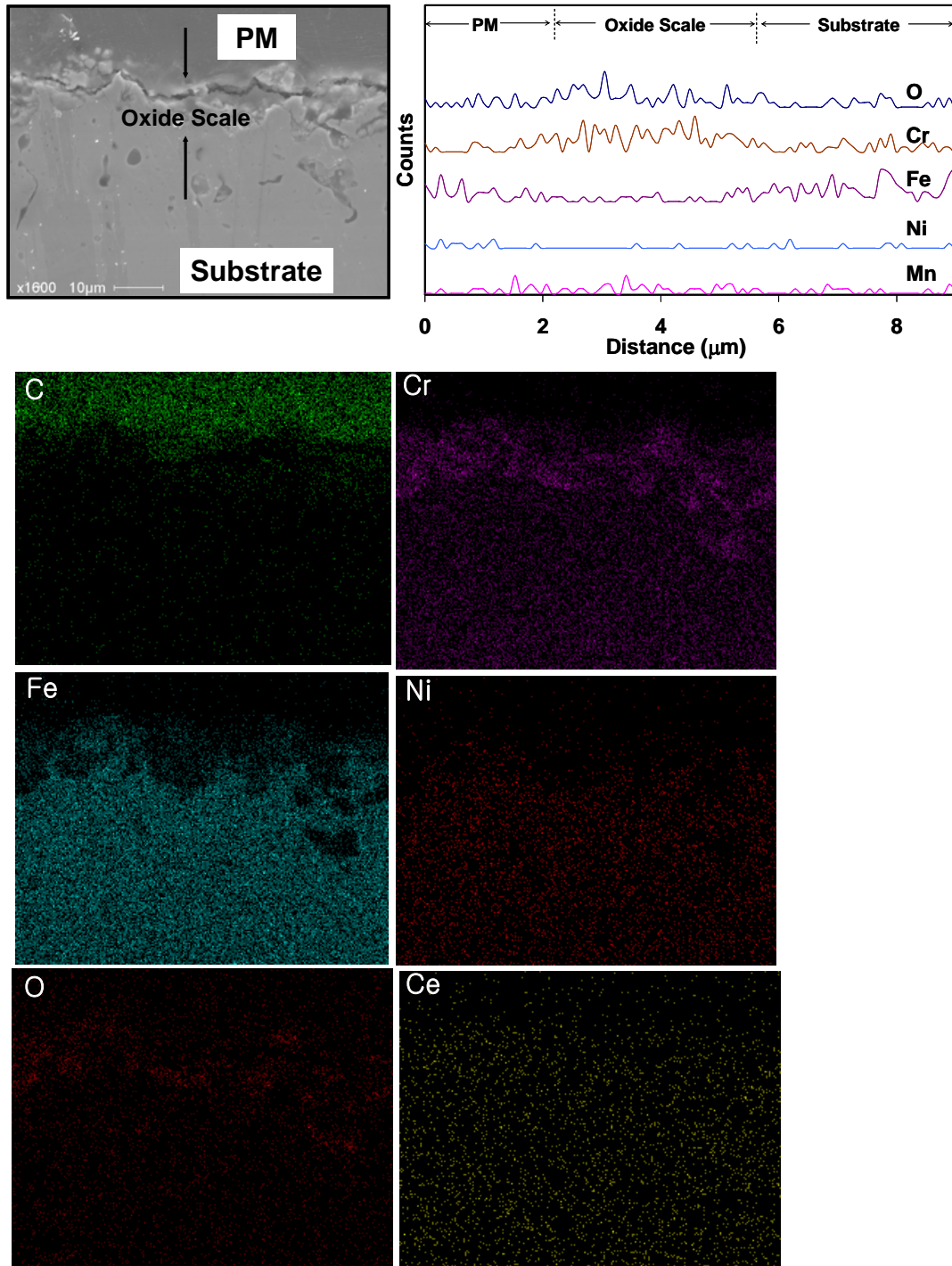


Figure 4.6 SEM micrograph of the cross section, line scanning and X-ray mapping of each element of SS samples coated with NC.

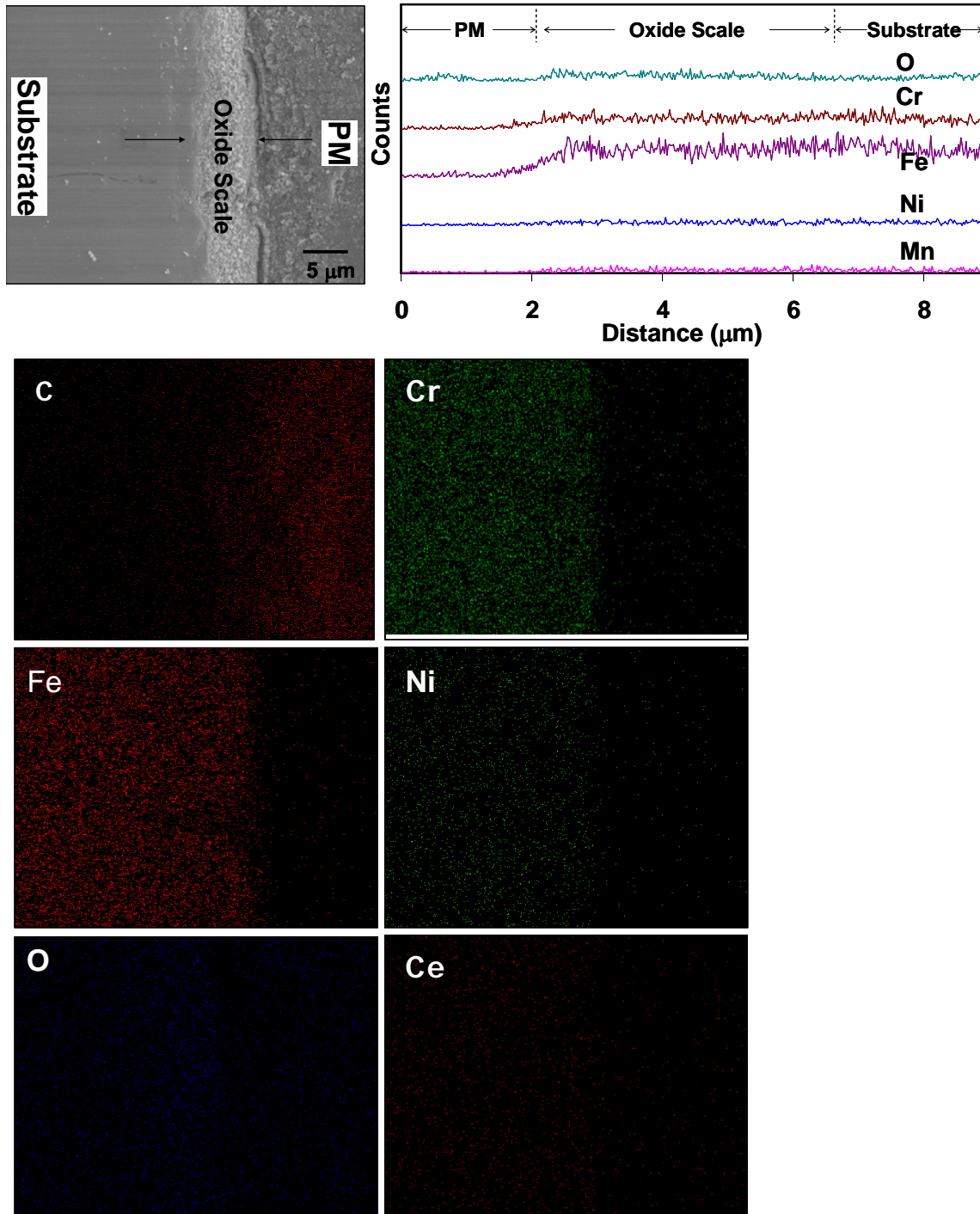


Figure 4.7 SEM micrograph of the cross section, line scanning and X-ray mapping of each element of SS samples coated with 20 LDN.

Cross section of NC and 20 LDN samples were analyzed in SEM for oxide layer thickness measurement and elemental mapping in the oxide scale. The oxide layer formed on NC sample is continuous and uniform with a thickness of 3-4 μm as shown in Figure 4.6. The scale formed on the 20 LDN sample is relatively discontinuous with a thickness of 6-8 μm as shown in the Figure 4.7. The oxide layer thickness of the uncoated sample is 30-35 μm and the thickness reduces more than 70% for both doped and undoped ceria samples when oxidized at 1243 K in dry air for 24 h. This showed a marked improvement in the NC based oxidation resistant coatings. The line scanning of NC sample showed more counts for Cr, Mn and no counts for Fe in the oxide scale as shown in Figure 4.6. This clearly showed the presence of chromia in the oxide layer. The x-ray mapping of NC sample cross section showed the presence of Cr in the oxide layer as shown in the Figure 4.6. This indicates the formation of the impervious chromia layer suppressing any diffusion of Fe outward, an important parameter for the development of oxidation resistant coatings. In the case of 20 LDN sample the counts for both iron and chromium are high in the oxide scale as shown in the Figure 4.7. The x-ray mapping of 20 LDN sample cross section showed the presence of Cr and Fe and also small amounts of Ni in the oxide layer as shown in the Figure 4.7. It indicates both iron oxide and chromia in the oxide layer formed on 20 LDN sample.

4.4.3 Phase Identification

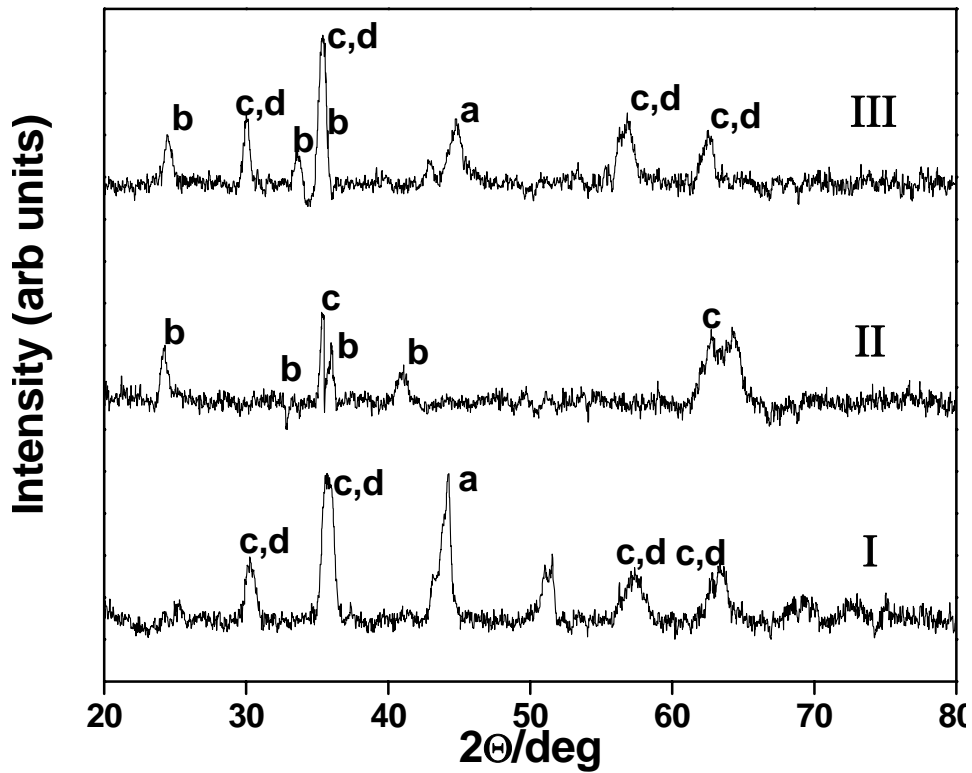


Figure 4.8 XRD spectra for SS surface (I) uncoated, (II) NC and (III) 20LDN coated samples. Peak identification: (a) Fe-Cr, (b) Cr_2O_3 , (c) Fe_3O_4 and (d) FeCr_2O_4 .

XRD is carried on the uncoated, NC and 20 LDN samples to identify the phases present in the top surface of the sample as shown in Figure 4.8. XRD on the uncoated sample after spalling showed the presence of Fe-Cr, Fe_3O_4 and FeCr_2O_4 . The presence of Fe-Cr peak in the SS sample shows the spalling of the oxide layer due to the difference in thermal expansion coefficients of the sample and oxide scale. The absence of the Fe-Cr peak in the case of the NC sample shows that there is no spalling of the oxide layer as well as the compactness of the oxide scale. The presence of this Fe-Cr peak is depressed in 20 LDN sample indicating a porous structure of the oxide layer. The XRD data further supports the SEM micrographs of the cross section (Figures

4.6 & 4.7), where the NC sample has a continuous, uniform oxide layer and the 20 LDN sample has a relatively porous oxide layer. The XRD pattern of the NC sample showed the primary presence of chromia and small amounts of iron oxide. The 20 LDN sample showed the presence of Fe_3O_4 , FeCr_2O_4 spinel peaks, and a less intense Cr_2O_3 peak. This shows the diffusion of Fe through the initial chromia layer and the formation of Fe_3O_4 , FeCr_2O_4 spinels on the top of the chromia layer. This may cause further degradation of the material by formation of voids at the interface between oxide scale and steel resulting in poor scale adherence upon subjection to long-term thermal cycling. However, in the current condition, no spalling of the oxide layer in the doped ceria samples is observed. This indicates that the diffusion of Fe through the chromium oxide is still minimal as compared to the SS and MC samples. To understand the diffusion kinetics, SIMS analysis was carried out on the oxide scales.

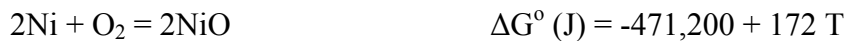
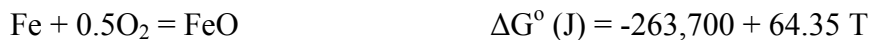
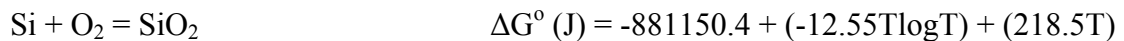
4.4.4 Diffusional Studies

In order to investigate the distribution of various alloying elements across the oxide scale, SIMS depth-profiling was carried out on the NC and 20 LDN coated-oxidized AISI 304 grade stainless steel samples at 1243 K for 24 h in dry air.

The formation of oxides at the surface of steel samples depends on both diffusion species (Fe, Cr, etc.) from the steel and oxygen supply to the interface. The diffusion of metal atoms towards the metal/oxide interface increases with increasing temperatures, while the supply of oxygen towards the gas/oxide interface increases with increasing oxygen vacancies present in the nanostructured coatings. Therefore, depending on the oxidation temperature and the oxygen availability, different oxide phases will form. The important feature of oxide formation is the

existence of a critical pressure (p'_c) of oxygen at specific oxidation temperature, where the supply of metal and oxygen to the interface are of an equal order of magnitude. It was observed that at a given temperature, a critical oxygen partial pressure is required to form a chromia enriched oxide layer ⁴⁶.

At any temperature if the number of metal atoms diffusing into the initial chromia layer is equal to the number of oxygen atoms available per unit time, then it can form the corresponding metal oxide. Thermodynamics plays an important role in explaining the formation of oxides under limited oxygen availability conditions. Considering Cr, Mn, Si, Fe and Ni can react with oxygen and the Standard Gibbs free energy of formation of the respective oxides is given by



The calculated free energy changes for Cr_2O_3 , MnO , SiO_2 , FeO , Fe_3O_4 and NiO are -528.7, -588.5, -657.85, -367.4, -360 and -257.4 kJ for one mole of oxygen to react with metal to form its oxide at 1243 K respectively. The negative values of ΔG° show that all of these oxides formation is feasible at 1243 K. But, formation of SiO_2 , MnO , and chromia are predominant when the supply of oxygen is limited. This indicates that when there are less oxygen vacancies, it

preferentially forms only chromia. However, when the oxygen vacancies are increased with La^{3+} doping, more number of oxygen atoms are available than the number of chromium atoms diffusing outward. All oxygen will react with chromium which has a higher free energy of oxide formation than iron⁴⁷. Thus, more the mobile iron⁴⁸ will segregate at the interface to react with oxygen during further oxidation. Hence, the film becomes more enriched in iron leaving the iron depletion zone behind. Similar results were observed when SS was oxidized at different partial pressures of oxygen, where at a lower oxygen partial pressure only chromia forms and at a higher partial pressures both chromia and iron oxides form⁴⁶.

The oxidation of SS at high temperatures results in the rapid formation of the oxide film mostly leading to a chromium depletion zone next to the oxide film because of a limited supply of chromium from the bulk alloy to its surface region. In that case, diffusion in the bulk alloy becomes the rate-limiting step for the oxide film growth. The depth profile of chromium in the NC sample did not reveal any depletion region near the metal/oxide interface, suggesting that the diffusion of chromium through the grain boundaries of the initial oxide layer is less than or equal to the diffusion of chromium in the underlying metal. So the diffusion of chromium, not in the bulk alloy but in the natural oxide layer, was the rate-limiting step for the oxide growth in the NC sample. Then, the growth rate of an oxide film is primarily controlled by the diffusion rate of chromium in the oxide layer as long as sufficient oxygen is available.

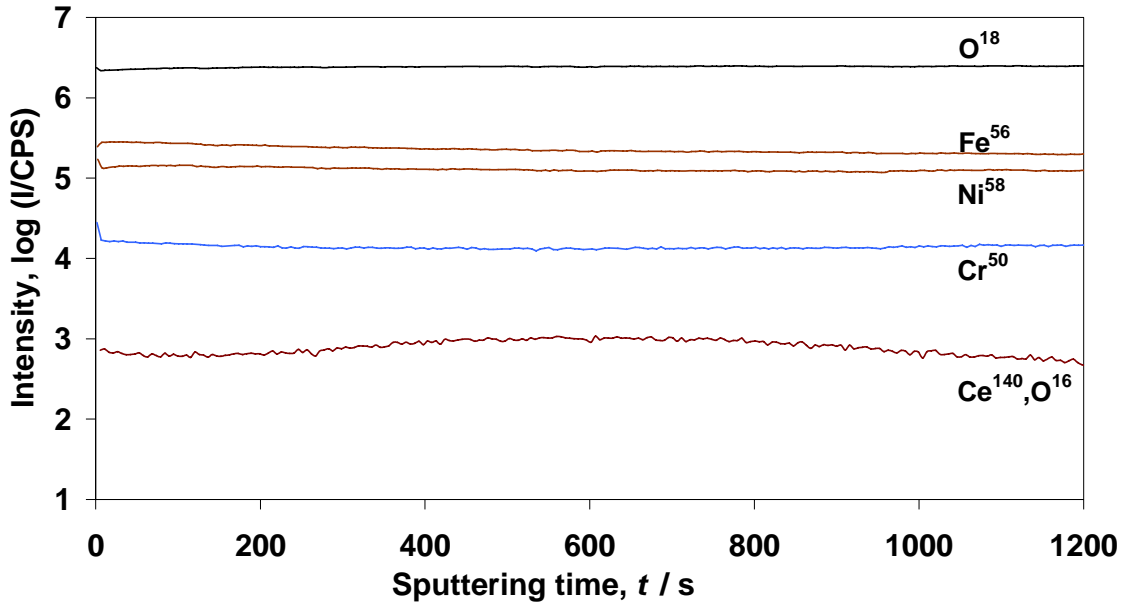


Figure 4.9 SIMS depth profiles of Fe, Ni, Cr and O from the outer surface to the inner surface of oxide scale formed on the NC coated SS.

The depth profile showed in Figure 4.9 exhibits higher counts of Cr in the oxide layer, which shows a gradual decrease in the chromium counts in this region, indicating the formation of a chromia layer on the surface. There is no change in the iron counts in this region showing no diffusion of Fe through the initial chromia layer formed. The constant counts of Fe, Cr and Ni after the gradual decrease in counts of these elements shows that the diffusion of these atoms are fast enough in the underlying metal. The variation in the concentration of iron, nickel and chromium indicates that there is no depletion of these elements inside the steel sample. This indicates that there is no void formation in the case of the NC sample. It shows that the sample is well protected after oxidizing in dry air for 24 h and can be subjected to further thermal cycles.

The diffusion coefficient D has been estimated by considering the concentration profiles of iron, chromium, and nickel measured by SIMS to the solution of Fick's law ⁴⁹. The concentration

profile $C(x,t)$ depends on the diffusion depth x and the annealing time t . The sputtering time in figure 6a and 6b is converted to depth x as diffusion depth is a product of rate of sputtering and sputtering time. The rate of sputtering used in these calculations is 0.666nm/sec.

The diffusion is based on the Fick's law:

$$\frac{\partial C(x,t)}{\partial t} = D \frac{\partial^2 C(x,t)}{\partial x^2}. \quad (12)$$

The shallow part of the profile can be well fitted by solution of Fick's second law.

$$C(z,t) - C_0 = (C_s - C_0) \left[1 - \operatorname{erf}\left(\frac{z}{2\sqrt{D_{\text{bulk}}t}}\right) \right] \quad (13)$$

From the concentration profiles of Fe, Ni and Cr with sputtering time shown in the figure 4.9 for the NC sample annealed at 1243 K in dry air for 24 h, the diffusivity of the elements were calculated by fitting the depth profiles into the solution to Fick's second law. The calculated diffusivity values for Ni, Fe, and Cr were 8.76×10^{-19} , 5.60×10^{-15} and 7.73×10^{-16} cm²/sec respectively. The low value of Ni diffusivity can also be observed in the figure 4.9, where there is very less variation of nickel concentration in the oxide layer.

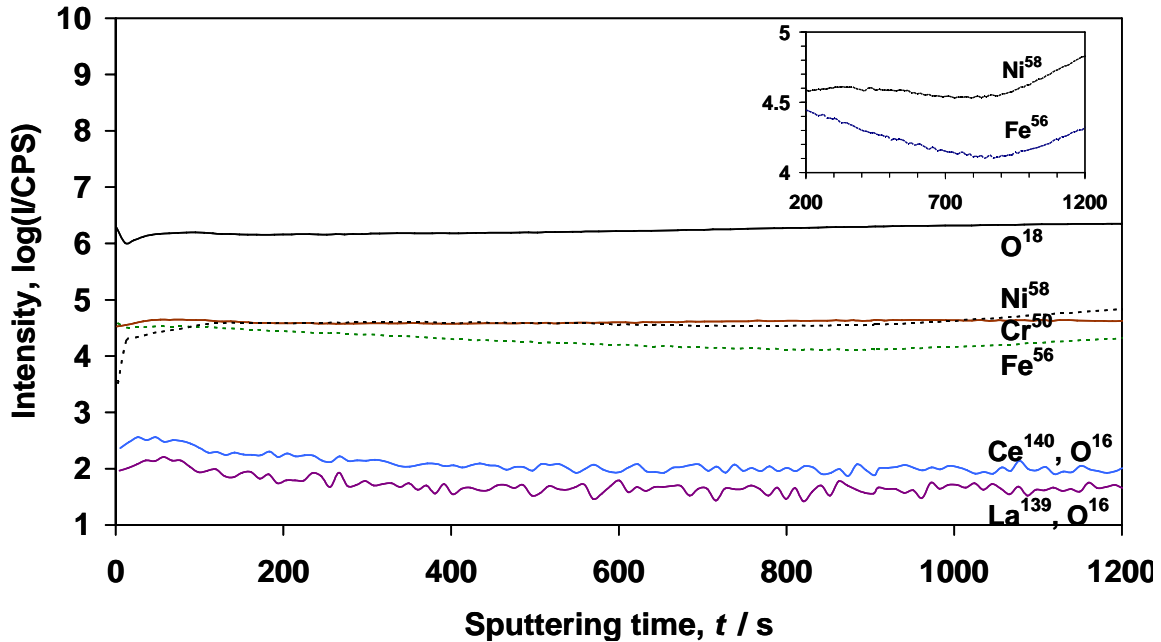


Figure 4.10 SIMS depth profiles of Fe, Ni and Cr from the outer surface to the inner surface of oxide scale formed on the 20 LDN coated SS. The inset shows Fe and Ni depletion zones present in the oxide layer.

The depth profile shown in Figure 4.10 exhibits higher counts of chromium compare to iron indicating that it is favorable to form chromia on the surface compare to iron oxide. It also showed an initial increase in chromium counts on the top of the oxide followed by constant number of counts indicates that the formation of chromia in top oxide scale. There is not much variation of chromium concentration up to one micron depth, indicating that the diffusion of chromium is fast enough in the underlying metal. There is gradual decrease in concentration of iron and nickel showing the depletion zones of Fe and Ni (Figure 4.10 inset). This shows that the diffusion of iron and nickel is very less in the underlying metal because of the impervious chromia layer formation.

From the concentration profiles of Fe, Ni, and Cr with depth shown in the Figure 4.10 for 20 LDN sample annealed at 1243 K in dry air for 24 h, the diffusivity of the elements were

calculated. The calculated diffusivity values for Ni, Fe, and Cr were 1.60×10^{-16} , 2.47×10^{-15} and 1.95×10^{-16} cm²/sec.

In brief, chromium rich oxide films grew below the NC coating as oxidation continued, but the composition of the oxide film was significantly changed by increasing the dopant concentration in the coating. As the diffusion rates depend exponentially on temperature, there exist a critical number of oxygen vacancies at which the supply of oxygen slightly exceeds the diffusion of chromium. Therefore, as the number of oxygen vacancies increases with increase of the dopant concentration, the formation of oxides other than chromia is also possible. The presence of Fe and Ni depletion zones in the case of 20 LDN indicates that the bulk diffusivity and diffusivity of these atoms in the oxide layer or coating differs.

4.5 Role of Oxygen Vacancies in High Temperature Protection

The lattice constant and oxygen vacancies increase with increasing amounts of trivalent elements such as La, Nd, etc ⁵⁰. The lattice expansion slope for trivalent ions doped in ceria is 0.3 for La³⁺ ions ⁸. Oxygen vacancies are created for replacement of each two Ce⁴⁺ sites by two La³⁺ ions to maintain electrostatic charge neutrality. The additions of La³⁺ ions to Ceria results in solid solutions of the form Ce_{1-x}La_xO_{2-y} that have the same fluorite structure that of Ceria.

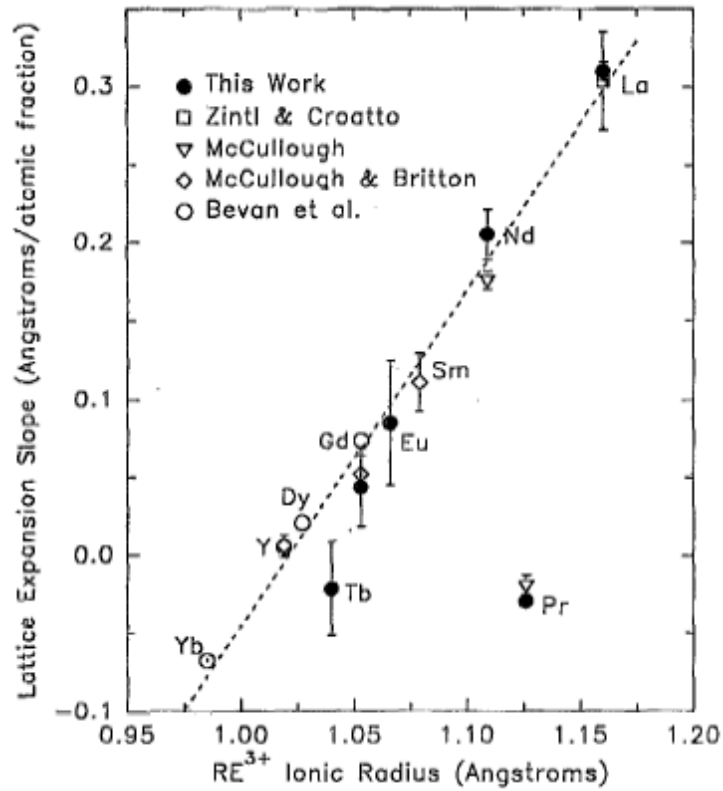
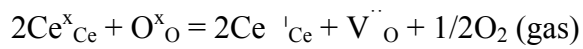
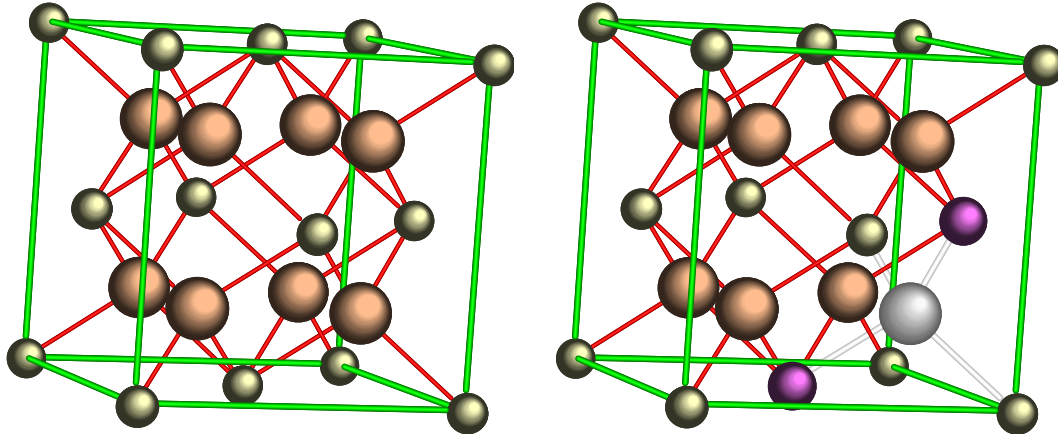


Figure 4.11 Lattice expansion slope vs. RE^{3+} ionic radius for $Ce_{1-x}RE_xO_{2-y}$ samples (J. R. McBride et al)

In CeO_{2-x} , loss of oxygen results in the generation of oxygen vacancies, which are compensated by generation of electrons. This reaction can be represented by the Kroger-Vink notation as:





where



Figure 4.12 Fluorite Structure of (a) Ceria (space-group: Fm3m) and (b) $Ce_{1-x}La_xO_{2-y}$ showing the increase in the lattice parameter and the presence of oxygen vacancies by doping La into nanocrystalline ceria.

The oxygen vacancy concentration of an oxide of type MO_{2-x} is equal to half of its deviation from stoichiometry (x).

$$N_{v,o} / N_o = [V_{\ddot{O}}] = x/2. \quad (14)$$

Table 4.2 Calculated oxygen vacancy concentration in ceria doped with lanthanum

Lanthanum doped Ceria	Oxygen vacancy concentration per lattice oxygen sites
2La Ceria ($\text{Ce}_{0.98}\text{La}_{0.02}\text{O}_{1.99}$)	0.005
20La Ceria ($\text{Ce}_{0.8}\text{La}_{0.2}\text{O}_{1.9}$)	0.05
40La Ceria ($\text{Ce}_{0.6}\text{La}_{0.4}\text{O}_{1.8}$)	0.1

At high temperature, diffusion of oxygen inward through the oxygen vacancies present in the ceria and doped ceria coatings determines the rate of initial oxidation. The availability of excess oxygen also enables further oxidation of Fe and Ni to form their oxides as well. As the oxygen vacancies increases with dopant concentration shown in the Table 4.2, the available oxygen increases with the increase of dopant concentration in the coating at high temperature.

The formation of a ceria-lanthana solid solution caused by dissolution of the La^{3+} ions into the Ceria lattice increases the lattice constant of lanthanum doped ceria because the radius of La^{3+} ion (1.19 Å) is larger than that of the Ce^{4+} ion (1.09 Å) ⁵¹. Since LDN contains more oxygen vacancies, the nucleation sites for chromia formation increase with the dopant concentration. This leads to the faster formation of initial protective chromia layer at the metal/coating interface, but also increases the grain boundary area of the chromia layer. The segregation of the NC and LDN at the grain boundaries of the chromia layer restricts the outward diffusion of

chromium and prefers inward diffusion of oxygen⁵². This can be seen from the oxidation kinetics plots (Figure 4.2), where a reduction of more than 90% weight gain in doped and undoped ceria samples compare to SS and MC coated sample is noted.

The formation of initial protective chromia layer on the surface of SS controls the rate of oxidation by outward diffusion of chromium through the grain boundary of chromia layer⁵³. The presence of grain boundary segregation is supportive of the hypothesis of blocking grain boundary transport by reactive element addition. This hypothesis assumes that large Ce^{4+} cations (ionic radii of 0.92\AA) form pairs with metal vacancies in oxide grain boundaries. The presence of dense arrays of such pairs inhibits metal cation diffusion, while allowing oxygen ion diffusion to continue. As a result, the change in the dominant oxide growth mechanism takes place from outward metal to inward oxygen diffusion, and the oxidation rate diminishes by 1-2 orders of magnitude. The presence of NC has significant grain boundary segregation effect on the chromia layer formed and protects at high temperature. As the dopant concentration increases the ease of chromia formation increases as well. This indicates more weight gain in the primary stage of oxidation (Figure 4.2). Increasing dopant concentration further refines the grains as evident from Figure 4.3.

The oxide scale growth mechanism in the cerium oxide particles is due to inward O_2 migration by the segregation of NC particles into the oxide grain boundaries and by blocking the outward diffusion of cations. Such a segregation effect in the case of NC is probably not only easier in terms of energetics but also faster than that of the micrometer-sized particles. The nanocrystalline particles, being 3 nm in size, can cover the substrate more uniformly and segregate Ce^{4+} ions into the grain boundaries more easily causing effective blockage of the

cation outward migration, thereby retarding the oxide scale growth rate of AISI 304 SS at 1243 K in dry air.

4.6 Conclusion

The high temperature oxidation kinetics of stainless steel samples showed that the weight gain per unit area of NC and LDN coatings is reduced more than 90% compared to uncoated and MC coatings. It also showed increase in weight gain per unit area for steel samples with increase in La concentration in LDN coatings. To further understand the role of oxygen vacancies in the formation of protective layer, the oxide layer is characterized by SEM, XRD and SIMS. Top surface morphology of oxide layer showed finer grain structure with increased porosity as the La concentration is increased in LDN coatings. Cross section of the NC, 20 LDN coated samples showed the thickness of oxide layer is 3-4 μm for NC sample where as the thickness of oxide layer is 6-8 μm . Both line and X-ray mapping showed the presence of only chromium (no iron) in the oxide layer indicating chromia rich oxide layer in NC coated sample. In the case of 20 LDN coated sample, the presence of both iron and chromium were observed indicating that the oxide layer consists of oxides of iron and chromium. X-Ray Diffraction of the top oxide scales shows the protective chromia in presence of nanoceria coated steels and absence of this peak in uncoated steel sample showed that the oxide is spalled off from the steel substrate. SIMS analysis on the NC sample showed the absence of depletion zones indicating no void formation and consequently better oxidation resistance at high temperature. In the case of 20 LDN sample, it showed the presence of Fe and Ni depletion zones indicating diffusion of these elements in oxide layer.

CHAPTER 5. CONCLUSIONS AND FUTURE WORK

5.1 Conclusion

Cerium Oxide nanoparticles with trivalent rare earth dopants have been analyzed to understand the effect of dopant size on the oxygen vacancy concentration and lattice parameter. Raman analysis of doped NC showed increase in oxygen vacancies by doping larger dopant (Sm^{3+} , Gd^{3+} and Y^{3+}) and variation of oxygen vacancy concentration is proportional to concentration of dopants. It also showed that doping of Yb^{3+} (smaller ionic radius compares to Ce^{4+} ion) in NC decreases the oxygen vacancy concentration. X-Ray Diffraction analysis showed presence of ceria peaks only. The absence of the additional peaks related to oxides of dopants indicates the formation of a single phase $\text{Ce}_{1-x}\text{RE}_x\text{O}_{2-y}$ type solid solution for the full doping range. It showed that there is lattice parameter change in NC by doping trivalent rare earth ions. It also showed that lattice parameter of NC increases by doping larger cations (Gd^{3+} and Y^{3+}) and decreases by doping smaller cation (Yb^{3+}). XPS analysis showed that there is a variation in Ce^{3+} to Ce^{4+} ratio by doping different trivalent elements. It showed that the ratio increases by doping larger ions (Gd^{3+} and Y^{3+}) and decreases by doping smaller ions (Yb^{3+}) compare to undoped nanoceria. HRTEM micrographs of NC and doped ceria (20 SDN, 20 GDN, 20 YDN and 20 YbDN) samples indicate uniform size (3-5 nm) of particles and also the diffraction pattern shows retaining of fluorite crystal structure of nanoceria even after doping larger or smaller trivalent ions in nanocrystalline cerium oxide lattice.

In order to study the role of oxygen vacancies in protection of stainless steel at high temperature, AISI 304 stainless steel samples were dip-coated with NC and LDN solutions synthesized by microemulsion method and annealed at 1243 K for 24h in dry air. The high temperature oxidation kinetics of 304 steels showed that the weight gain per unit area of NC and LDN coatings is reduced significantly (2-4 orders of magnitude decrease in k_p) when compared to uncoated and MC coatings. SEM micrographs of the top oxide layer showed finer grain structure with increased porosity as the La concentration is increased in LDN coatings. XRD of the oxide scales shows the protective chromia in presence of nanoceria coated steels. SIMS analysis on the NC sample showed the absence of depletion zones indicating no void formation and consequently better oxidation resistance at high temperature. This study confirms the change in oxide growth mechanism from cation outward to oxygen inward and also shows that increase in partial pressure of oxygen by increase in oxygen vacancies in nanocrystalline ceria coatings changes the oxide scale to more enrich in iron.

5.2 Future Work

From the current study, it is easily understood that the oxygen vacancy concentration depends on dopant size and its concentration in nanocrystalline cerium oxide. This work also showed that oxygen vacancy concentration is critical to form chromia enriched oxide scale. So from the above study, it is easy to identify the type of dopant and its concentration in nanocrystalline cerium oxide which supplies the critical oxygen partial pressure required at high temperature to form primarily impervious chromia layer. It also gives an idea of selectivity of dopant to optimize the catalytic applications of nanocrystalline cerium oxide.

REFERENCES

1. Chengyun, W. et al. A novel method to prepare nanocrystalline (7 nm) ceria. *Materials Science and Engineering B* 39, 160-162 (1996).
2. Djuricic, B. & Pickering, S. Nanostructured cerium oxide: preparation and properties of weakly-agglomerated powders. *Journal of the European Ceramic Society* 19, 1925-1934 (1999).
3. Czerwinski, F. & Szpunar, J. A. The nanocrystalline ceria sol-gel coatings for high temperature applications. *Journal of Sol-Gel Science and Technology* 9, 103-114 (1997).
4. Masui, T. et al. Characterization and catalytic properties of CeO₂-ZrO₂ ultrafine particles prepared by the microemulsion method. *Journal of Alloys and Compounds* 269, 116-122 (1998).
5. Wu, Z. et al. EXAFS study on the local atomic structures around Ce in CeO₂ nanoparticles. *Materials Science and Engineering A* 286, 179-182 (2000).
6. Kawai, T., Usui, Y. & Kon-No, K. Synthesis and growth mechanism of GeO₂ particles in AOT reversed micelles. *Colloids and Surfaces A: Physicochemical and Engineering Aspects* 149, 39-47 (1999).
7. Mayo, M. J. Synthesis and applications of nanocrystalline ceramics. *Materials & Design* 14, 323-329 (1993).
8. McBride, J. R., Hass, K. C., Poindexter, B. D. & Weber, W. H. Raman and X-Ray Studies of Ce_{1-x}Re_xO_{2-y}, Where Re=La, Pr, Nd, Eu, Gd, and Tb. *Journal of Applied Physics* 76, 2435-2441 (1994).
9. Weber, W. H., Hass, K. C. & McBride, J. R. Raman-Study of CeO₂ - 2nd-Order Scattering, Lattice-Dynamics, and Particle-Size Effects. *Physical Review B* 48, 178-185 (1993).
10. Deshpande, S., Patil, S., Kuchibhatla, S. V. & Seal, S. Size dependency variation in lattice parameter and valency states in nanocrystalline cerium oxide. *Applied Physics Letter* 87, 1331-1333 (2005).
11. Seal, S. & Barr, T. *Experimental Methods in the Physical Sciences*. Academic, New York, 111-190 (2001).
12. Antill, J. & Peakall, K. Influence of an alloy addition of yttrium on the oxidation behavior of an austenitic and a ferritic SS in carbon dioxide. *Journal of Iron Steel Institute* 205, 1136-1142 (1967).

13. Stringer, J. The Reactive Element Effect in High-Temperature Corrosion. *Materials Science and Engineering a-Structural Materials Properties Microstructure and Processing* 120, 129-137 (1989).
14. Stringer, J., Wallwork, G. R., Wilcox, B. A. & Hed, A. Z. Effect of a Thoria Dispersion on High-Temperature Oxidation of Chromium. *Corrosion Science* 12, 625-& (1972).
15. Tien, J. K. & Pettit, F. S. Mechanism of Oxide Adherence on Fe-25cr-4al (Y or Sc) Alloys. *Metallurgical Transactions* 3, 1587-& (1972).
16. Cocking, J. L., Sprague, J. A. & Reed, J. R. Oxidation behaviour of ion-implanted NiCrAl. *Surface and Coating Technology* 36, 133-142 (1988).
17. George, P. J., Bennett, M. J., Bishop, H. E., Cotell, C. M. & Garratt-Reed, A. J. Secondary ion mass spectrometry and scanning transmission and transmission electron microscopy studies of the effects of reactive elements on nickel oxidation. *Surface and Coatings Technology* 51, 45-51 (1992).
18. George, P. J., Bennett, M. J., Bishop, H. E. & Dearnaley, G. The effects of ion implantation upon nickel oxidation investigated by secondary ion mass spectrometry. *Materials Science and Engineering A* 116, 111-117 (1989).
19. Paul, A., Elmabet, S. & Odriozola, J. A. Low cost rare earth elements deposition method for enhancing the oxidation resistance at high temperature of Cr₂O₃ and Al₂O₃ forming alloys. *Journal of Alloys and Compounds* 323-324, 70-73 (2001).
20. Wei, F. I. & Stott, F. H. The development of Cr₂O₃ scales on iron-chromium alloys containing reactive elements. *Corrosion Science* 29, 839-861 (1989).
21. Yu, X. Q. & Sun, Y. S. The oxidation improvement of Fe₃Al based alloy with cerium addition at temperature above 1000⁰C. *Materials Science and Engineering A* 363, 30-39 (2003).
22. Giggins, C. S., Kear, B. H., Pettit, F. S. & Tien, J. K. Factors Affecting Adhesion of Oxide Scales on Alloys. *Metallurgical Transactions* 5, 1685-1688 (1974).
23. Duffy, D. M. & Tasker, P. W. Theoretical-Studies of Diffusion-Processes Down Coincident Tilt Boundaries in Nio. *Philosophical Magazine a-Physics of Condensed Matter Structure Defects and Mechanical Properties* 54, 759-771 (1986).
24. Seal, S., Roy, S. K., Bose, S. K. & Kuiry, S. C. Ceria based high temperature coatings for oxidation prevention. *Journal of Materials* 52, 1-8 (2000).
25. Moon, D. P. & Bennett, M. J. The effects of reactive element oxide coatings on the oxidation behavior of metals and alloys at high temperature. *Materials Science Forum* 43, 269-298 (1989).

26. Spanier, J. E., Robinson, R. D., Zheng, F., Chan, S. W. & Herman, I. P. Size-dependent properties of CeO_{2-y} nanoparticles as studied by Raman scattering. *Physical Review B* 64 (2001).
27. Tsunekawa, S., Sivamohan, R., Ito, S., Kasuya, A. & Fukuda, T. Structural study on monosize CeO_{2-x} nano-particles. *Nanostructured Materials* 11, 141-147 (1999).
28. Zhang, F. et al. Cerium oxide nanoparticles: Size-selective formation and structure analysis. *Applied Physics Letters* 80, 127-129 (2002).
29. Tsunekawa, S. et al. in *Rare Earths '98* 439-445 (1999).
30. Aneggi, E., Boaro, M., Leitenburg, C. d., Dolcetti, G. & Trovarelli, A. Insights into the redox properties of ceria-based oxides and their implications in catalysis. *Journal of Alloys and Compounds* 408-412, 1096-1102 (2006).
31. Demoulin, O., Navez, M., Mugabo, J. L. & Ruiz, P. The oxidizing role of CO₂ at mild temperature on ceria-based catalysts. *Applied Catalysis B: Environmental* 70, 284-293 (2007).
32. Nolan, M., Fearon, J. E. & Watson, G. W. Oxygen vacancy formation and migration in ceria. *Solid State Ionics* 177, 3069-3074 (2006).
33. Nolan, M., Parker, S. C. & Watson, G. W. The electronic structure of oxygen vacancy defects at the low index surfaces of ceria. *Surface Science* 595, 223-232 (2005).
34. Trovarelli, A., Boaro, M., Rocchini, E., de Leitenburg, C. & Dolcetti, G. Some recent developments in the characterization of ceria-based catalysts. *Journal of Alloys and Compounds* 323-324, 584-591 (2001).
35. Ecer, G. M., Singh, R. B. & Meier, G. H. The Influence of Superficially applied oxide powders on the high-temperature oxidation behavior of Cr₂O₃-forming alloys. *Oxidation of Metals* 18, 55-81 (1982).
36. Seal, S., Bose, S. K. & Roy, S. K. Improvement in the Oxidation Behavior of Austenitic Stainless-Steels by Superficially Applied, Cerium Oxide Coatings. *Oxidation of Metals* 41, 139-178 (1994).
37. Czerwinski, F. & Smeltzer, W. W. The Growth and Structure of Thin Oxide-Films on Ceria-Sol-Coated Nickel. *Oxidation of Metals* 40, 503-527 (1993).
38. Patil, S., Kuiry, S. C. & Seal, S. Nanocrystalline ceria imparts better high-temperature protection. *Proceedings of the Royal Society of London Series a-Mathematical Physical and Engineering Sciences* 460, 3569-3587 (2004).
39. Czerwinski, F. & Szpunar, J. A. Optimizing properties of CeO₂ sol-gel coatings for protection of metallic substrates against high temperature oxidation. *Thin Solid Films* 289, 213-219 (1996).

40. Seal, S., Kuiry, S. C. & Bracho, L. A. Studies on the surface chemistry of oxide films formed on IN-738LC superalloy at elevated temperatures in dry air. *Oxidation of Metals* 56, 583-603 (2001).
41. Tedmon, C. S. Effect of Oxide Volatilization on Oxidation Kinetics of Cr and Fe-Cr Alloys. *Journal of the Electrochemical Society* 113, 766-& (1966).
42. Huntz, A. M. Diffusion in Growing Oxide Scale. *Journal De Physique Iii* 5, 1729-1757 (1995).
43. Atkinson, A. Transport Process during the growth of oxide films at elevated temperature. *Reviews of Modern Physics* (1985).
44. Saraf, L. et al. Oxygen Diffusion in Nanocrystals in CeO₂. *IEEE* (2003).
45. Sabioni, A. C. S., Huntz, A., da Luz, E. C., Mantel, M. & Haut, C. Comparative Study of High Temperature Oxidation Behavior in AISI 304 and AISI 439 Stainless Steels. *Materials Research* 6, 179-185 (2003).
46. Cho, B., Moon, S. & Chung, S. Characterization of diffusion properties of chromium in stainless-steel oxides by photoemission spectroscopy. *Journal of Vacuum Science and Technology. A* 3, 19 (1991).
47. Lince, J. R., Didziulis, S. V., Shuh, D. K., Durbin, T. D. & Yarmoff, J. A. Interaction of O₂ with the Fe_{0.84}Cr_{0.16}(001) Surface Studied by Photoelectron-Spectroscopy. *Surface Science* 277, 43-63 (1992).
48. Allen, G. C., Dyke, J. M., Harris, S. J. & Morris, A. A Surface Study of the Oxidation of Type-304L Stainless-Steel at 600-K in Air. *Oxidation of Metals* 29, 391-408 (1988).
49. Sakai, N., Yamaji, K., Horita, T., Negishi, H. & Yokokawa, H. Chromium diffusion in lanthanum chromites. *Solid State Ionics* 135, 469-474 (2000).
50. Patil, S., Seal, S., Guo, Y., Schulte, A. & Norwood, J. Role of trivalent La and Nd dopants in lattice distortion and oxygen vacancy generation in cerium oxide nanoparticles. *Applied Physics Letters* 88 (2006).
51. Sun, K., Lu, W., Wang, M. & Xianlunxu. Characterization and catalytic performances of La doped Pd/CeO₂ catalysts for methanol decomposition. *Applied Catalysis A* 268, 107-113 (2004).
52. Papaioacovou, P., Hussey, R. J., Mitchell, D. F. & Graham, M. J. The effect of CeO₂ coatings on the oxidation behaviour of Fe-20Cr alloys in O₂ at 1173 K. *Corrosion Science* 30, 451-455 (1990).
53. Peng, X., Yan, J., Zhou, Y. & Wang, F. Effect of grain refinement on the resistance of 304 stainless steel to breakaway oxidation in wet air. *Acta Materialia* 53, 5079-5088 (2005).